

Beamfocusing Capabilities of a Uniform Linear Array in the Holographic Regime

Xavier Mestre, *Senior Member, IEEE*, Adrian Agustin, *Senior Member, IEEE*

Abstract—The use of multiantenna technologies in the near field offers the possibility of focusing the energy in spatial regions rather than just in angle. The objective of this paper is to provide a formal framework that allows to establish the region in space where this effect can take place and how efficient this focusing can be, assuming that the transmit architecture is a uniform linear array (ULA). A dyadic Green's channel model is adopted, and the amplitude differences between the receiver and each transmit antenna are effectively incorporated in the model. By considering a second-order expansion of the signal to noise ratio (SNR) around the intended receiver, a formal criterion is derived in order to establish whether beamfocusing is feasible or not. For the regions where beamfocusing is indeed possible, an analytic description is provided that determines the shape and position of the asymptotic ellipsoid where a minimum SNR is achieved. Further insights are provided by considering the holographic regime, whereby the number of elements of the ULA increase without bound while the distance between adjacent elements converges to zero. This asymptotic framework allows to simplify the analytical form of the beamfocusing feasibility region, which in turn provides some further insights into the shape of the coverage regions depending on the position of the intended receiver. In particular, it is shown that beamfocusing is only possible if the size of the ULA is at least 4.4λ where λ is the transmission wavelength. Furthermore, a closed form analytical expression is provided that asymptotically determines the maximum distance where beamfocusing is feasible as a function of the elevation angle. In particular, beamfocusing is only feasible when the receiver is located between a minimum and a maximum distance from the array, where these upper and lower distance limits effectively depend on the angle of elevation.

Index Terms—Holographic arrays, near-field communications, beamfocusing, extra large antenna arrays.

I. INTRODUCTION

Modern wireless communication systems heavily depend on multi-antenna technology to maximize performance in terms of reliability and throughput. As these systems shift to higher frequency bands, such as millimeter wave (mmWave) and sub-terahertz (THz) frequencies [1], [2], multi-antenna technology becomes crucial for overcoming the more challenging propagation conditions. These higher frequency bands are characterized by significant propagation losses and increased material absorption, leading to communication channels with a

dominant line-of-sight component. This introduces challenges for traditional multi-antenna signal processing techniques, which must be redesigned in order to effectively utilize the inherent structure of these channels. Simultaneously, the adoption of extra-large antenna arrays is growing to satisfy the high-performance requirements of future wireless networks. These extensive antenna setups are approaching the size of the transmitter-receiver distance, which is itself being reduced to mitigate high propagation losses. This marks a fundamental shift from conventional wireless architectures, which typically assume operation in the far field. In these evolving scenarios, the assumption of planar electromagnetic wave fronts is no longer valid, necessitating the adoption of more sophisticated near-field channel models. Interestingly, this near-field structure offers potential performance advantages in line-of-sight conditions [3]–[6].

One of the main advantages of operating in the near field is the fact that spatial filters may be used to do *beamfocusing*, as opposed to conventional beamforming (in the far field). This typically refers to the capability of focusing the energy of the transmitted signal towards a specific spatial location rather than just an angular direction (as beamforming). In other words, a spatial filter may be designed so that it targets a specific point in space [7]–[10] rather than just a direction of radiation. This opens up the possibility of multiplexing communications not only in angle but also in location, so that multiple user equipments could in principle share the same radio link even if they are all seen from the same direction of arrival [11], [12].

A lot of research has recently taken place aimed at the characterization of the beamfocusing phenomenon. Most of the literature has been focused on the characterization of the spatial region where beamfocusing is feasible (i.e. the beamfocusing feasibility region) as well as the determination of the spatial resolution of the spatial response (both in angle and depth). Research so far has considered simplified channel models that essentially disregard the amplitude variations across the array [13], [14], an approximation that is less valid when the dimensions of the array are comparable in magnitude with the propagation distance. This assumption is dropped in the present contribution, where a slightly more general channel model based on the Green function is adopted. This is inspired by work in [15], which considers a multi-user MIMO setting based on a channel model with three spatial polarizations based on the Green dyadic function. This channel model has also been recently proposed in [16] to analyze the capacity of holographic surfaces composed of densely-packed surface radiators with arbitrary placements, as well as in [17], where

This work is supported by the grant from the Spanish ministry of economic affairs and digital transformation and of the European union - NextGenerationEU UNICO-5G I+D/AROMA3D-Earth and AROMA3D-Hybrid (TSI-063000-2021-69 and TSI-063000-2021-71), by Grant 2021 SGR 00772 funded by the Universities and Research Department from Generalitat de Catalunya, and by the Spanish Government through the project 6G AI-native Air Interface (6G-AINA, PID2021-128373OB-I00 funded by MCIN/AEI/10.13039/501100011033) ERDF A way of making Europe.

infinitesimal dipoles with three orthogonal polarizations were considered on both ends of the communication link.

The Green dyadic channel model [18] represents the situation in which the radiating elements are composed of up to three orthogonal infinitesimal dipoles. This can be taken as an approximation of a more realistic situation in which the radiating elements have a more complicated radiation pattern. It can also be used to model the behavior of arrays of metasurface antennas [19]–[23]. These are the basic implementation of holographic apertures [16], [24]–[27], also known as continuous aperture architectures [28], [29] or large intelligent surfaces [30] in the array processing literature. Holographic apertures act as a continuous antenna array, dynamically shaping and controlling signal generation and electromagnetic wave projection, effectively creating "holograms" of electromagnetic fields [26]. The behavior of such holographic apertures can be accurately modeled by considering an asymptotically large number of antennas with an asymptotically small inter-element spacing. This approach treats the array aperture as a continuum of radiating elements capable of manipulating electromagnetic waves at the most fundamental physical level.

The present paper builds upon the approach in [31], which proposed the use of the asymptotic holographic description of a general uniform planar array to characterize the achievable rate of a single-user channel employing multiple polarizations. In this paper, we will employ the same channel model and approach in order to further investigate the beamfocusing capabilities of a ULA in the holographic regime. The study allows to conclude that beamfocusing is only possible when the total length of the ULA is at least 4.4λ where λ is the transmission wavelength. Simple analytical formulas are also provided that allow to describe the range of distances where beamfocusing is possible for each given elevation angle.

II. SCENARIO AND SIGNAL MODEL

Consider a downlink transmission from a uniform linear array (ULA) towards a certain intended receiver¹. The transmit ULA is composed of $2M + 1$ elements placed along the y -axis with an interelement separation of Δ_T meters, see further Fig. 1. Each element of the ULA consists of up to three infinitesimal dipoles aligned with the three cartesian coordinates. We will denote as t_{pol} the number of polarizations employed at the transmit array, so that when $t_{\text{pol}} = 1$ (resp. $t_{\text{pol}} = 2$, $t_{\text{pol}} = 3$) each ULA element employs one (resp. two, three) linear polarizations along the x -axis (resp. x , y -axes, x , y , z -axes).

Let us now consider the case where only one symbol stream is transmitted, and the whole transmit array is used to focalize the energy towards a certain point with cartesian coordinates $\mathbf{r}_0 \in \mathbb{R}^3$. The signal model at a certain point with coordinates $\mathbf{r} \in \mathbb{R}^3$ can be expressed as

$$\mathbf{y} = \mathbf{H}_{\text{pol}}(\mathbf{r}) \mathbf{w}x + \mathbf{n}$$

where \mathbf{w} is the unit norm transmit spatial filter, of dimensions $(2M + 1)t_{\text{pol}}$, x is the transmit signal and \mathbf{n} is the noise

¹Note that most of the conclusions also hold in the reverse (uplink) situation due to the symmetry of the problem.

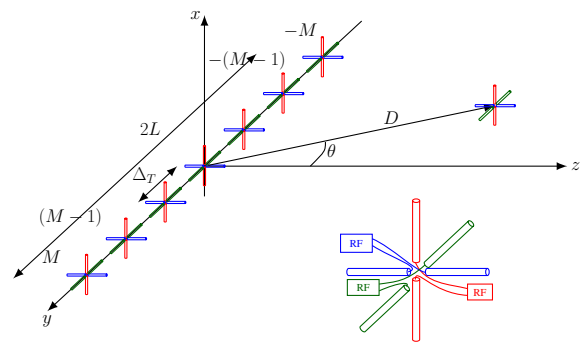


Fig. 1. Scenario configuration. The transmitter is a ULA consisting of $2M + 1$ elements, each incorporating 3 orthogonal infinitesimal dipoles. It is assumed that at least the polarization in the x -axis (red dipoles) is employed at the transmitter. Here, D is the distance between the receiver and the center of the array, θ is the elevation angle.

vector (with zero mean and power σ^2). We will assume that the receiver consists of three infinitesimal dipoles that are independently downconverted/sampled, so that both \mathbf{y} and \mathbf{n} have dimensions $r_{\text{pol}} = 3$ in this study. The channel matrix $\mathbf{H}_{\text{pol}}(\mathbf{r})$ can be decomposed as

$$\mathbf{H}_{\text{pol}}(\mathbf{r}) = \left[\mathbf{H}_{-M}^{t_{\text{pol}} \times r_{\text{pol}}}(\mathbf{r}), \dots, \mathbf{H}_M^{t_{\text{pol}} \times r_{\text{pol}}}(\mathbf{r}) \right] \quad (1)$$

where $\mathbf{H}_m^{t_{\text{pol}} \times r_{\text{pol}}}(\mathbf{r}) = [\mathbf{H}_m(\mathbf{r})]_{1:r_{\text{pol}}, 1:t_{\text{pol}}}$ and where $\mathbf{H}_m(\mathbf{r})$ is a 3×3 channel matrix between the three polarizations at the m th element of the ULA and the three polarizations at the receiver. Disregarding the reactive terms and considering only the radiative electromagnetic field, the channel model can be expressed as $\mathbf{H}_m(\mathbf{r}) = h_m(\mathbf{r}) \mathbf{P}_m^\perp(\mathbf{r})$ with

$$h_m(\mathbf{r}) = \frac{\xi}{\lambda} \frac{1}{\|\mathbf{r} - \mathbf{p}_m\|} \exp\left(-j \frac{2\pi}{\lambda} \|\mathbf{r} - \mathbf{p}_m\|\right) \quad (2)$$

where ξ is a certain complex constant², λ is the transmission wavelength, \mathbf{p}_m is position vector of the m th element of the ULA and where $\mathbf{P}_m^\perp(\mathbf{r})$ is the orthogonal projection matrix

$$\mathbf{P}_m^\perp(\mathbf{r}) = \mathbf{I}_3 - \mathbf{P}_m(\mathbf{r}), \quad \mathbf{P}_m(\mathbf{r}) = \frac{(\mathbf{r} - \mathbf{p}_m)(\mathbf{r} - \mathbf{p}_m)^T}{\|\mathbf{r} - \mathbf{p}_m\|^2}.$$

Consider the singular value decomposition

$$\frac{1}{\sqrt{2M + 1}} \mathbf{H}_{\text{pol}}(\mathbf{r}_0) = \mathbf{U} \mathbf{\Sigma}^{1/2} \mathbf{V}^H.$$

Let \mathbf{u} and \mathbf{v} respectively denote the left and right singular vector associated to the maximum singular value. It is well known that the transmit filter $\mathbf{w} = \mathbf{v}$ is the one that maximizes the SNR at a receiver located at $\mathbf{r} = \mathbf{r}_0$. We will assume from now on that this is the spatial filter that is used at the transmit side.

Assume that the transmit power is fixed to $\mathbb{E}|x|^2 = \bar{P}/(2M + 1)$, i.e. it decreases linearly with the number of transmit antennas. We define the received signal to noise ratio at the position \mathbf{r} as

$$\text{SNR}(\mathbf{r}) = \bar{P} \frac{\mathbf{w}^H \mathbf{H}_{\text{pol}}^H(\mathbf{r}) \mathbf{H}_{\text{pol}}(\mathbf{r}) \mathbf{w}}{\sigma^2 (2M + 1)}. \quad (3)$$

²If the channel is considered to be proportional to the electromagnetic field, the constant ξ can be seen to be proportional to the permittivity of the medium.

In particular, $\text{SNR}(\mathbf{r}_0)$ is the SNR at the intended location, that is

$$\text{SNR}(\mathbf{r}_0) = \frac{\bar{P}\lambda_{\max}}{\sigma^2}$$

where λ_{\max} is the maximum eigenvalue of $\mathbf{H}_{\text{pol}}(\mathbf{r}_0)\mathbf{H}_{\text{pol}}^H(\mathbf{r}_0)/(2M+1)$. The objective of this paper is to study how $\text{SNR}(\mathbf{r})$ behaves near the intended position \mathbf{r}_0 . To that effect, we will carry out a perturbation analysis of $\text{SNR}(\mathbf{r})$ around this point. We will say that beamfocusing is feasible at \mathbf{r}_0 when $\text{SNR}(\mathbf{r})$ decays locally as we move away from the intended position. Hence, the beamfocusing feasibility region is defined as the region of points in space such that $\text{SNR}(\mathbf{r})$ behave as a locally concave function. This approach is different from previous studies, which focused on the characterization of the *global* spatial response. Our approach is, in this sense, eminently local.

Remark 1. Here and throughout this paper we will need to bound a number of error terms by quantities that are not altered when considering the holographic regime (that is when the distance between infinitesimal dipoles goes to zero). To that effect, we define a “nice constant” as a constant that depends only on the quantities $|\xi|$, \bar{P} , σ^2 , λ . In particular, a nice constant does not depend on the transmit antenna index (m), the number of elements of the ULA (M), the position of the different array elements at the ULA (\mathbf{p}_m) or the position of the receiver (\mathbf{r} , \mathbf{r}_0). Likewise, we define a nice polynomial as a polynomial whose coefficients are nice constants. Throughout the paper, nice polynomials will generally be denoted as $P(\cdot)$. Note, however, that the actual value of the polynomial may vary from one line to another.

The following proposition establishes a second order Taylor series approximation of the channel matrix. We will use the definition of nice polynomial above to provide a bound on the reminder term that will be employed later on. The objective of this bound is to ensure that the error associated to the reminder term in the expansion does not scale up when considering the holographic approximation.

Proposition 1. The channel matrix $\mathbf{H}_m(\mathbf{r})$ accepts the following Taylor expansion around $\mathbf{r} = \mathbf{r}_0$

$$\mathbf{H}_m(\mathbf{r}) = \mathbf{H}_m(\mathbf{r}_0) + \mathcal{G}_m(\Delta_r) + \mathcal{H}_m(\Delta_r) + \mathcal{R}_m(\bar{\mathbf{r}}, \Delta_r)$$

where $\Delta_r = (\mathbf{r} - \mathbf{r}_0) = [\Delta_x, \Delta_y, \Delta_z]^T$ and where $\bar{\mathbf{r}}$ is in the segment joining \mathbf{r} and \mathbf{r}_0 . The three matrices $\mathcal{G}_m(\Delta_r)$, $\mathcal{H}_m(\Delta_r)$ and $\mathcal{R}_m(\bar{\mathbf{r}}, \Delta_r)$ respectively correspond to the gradient, Hessian and reminder terms, and can be described as follows. The gradient term $\mathcal{G}_m(\Delta_r)$ takes the form

$$\begin{aligned} \mathcal{G}_m(\Delta_r) = & - \left(1 + j \frac{2\pi}{\lambda} \|\mathbf{r}_{m,0}\| \right) \frac{\Delta_r^T \mathbf{r}_{m,0}}{\|\mathbf{r}_{m,0}\|^2} \mathbf{H}_m(\mathbf{r}_0) \quad (4) \\ & - \frac{\mathbf{r}_{m,0} \Delta_r^T}{\|\mathbf{r}_{m,0}\|^2} \mathbf{H}_m(\mathbf{r}_0) - \mathbf{H}_m(\mathbf{r}_0) \frac{\Delta_r \mathbf{r}_{m,0}^T}{\|\mathbf{r}_{m,0}\|^2} \end{aligned}$$

where $\mathbf{r}_{m,0} = \mathbf{r}_0 - \mathbf{p}_m$. The Hessian term $\mathcal{H}_m(\Delta_r)$ can be expressed as

$$\begin{aligned} \mathcal{H}_m(\Delta_r) = & \frac{h_m(\mathbf{r}_0)}{\|\mathbf{r}_{m,0}\|^2} \left[\Xi_{1,0} + \left(1 + j \frac{2\pi}{\lambda} \|\mathbf{r}_{m,0}\| \right) \Xi_{2,0} \right. \\ & \left. + \left(1 + j \frac{2\pi}{\lambda} \|\mathbf{r}_{m,0}\| \right)^2 \Xi_{3,0} \right] \quad (5) \end{aligned}$$

where the three matrices $\Xi_{1,0}$, $\Xi_{2,0}$, $\Xi_{3,0}$ take the form

$$\begin{aligned} \Xi_{1,0} = & -2\mathbf{P}_m^\perp(\mathbf{r}_0)\Delta_r\Delta_r^T\mathbf{P}_m^\perp(\mathbf{r}_0) \\ & + 2\mathbf{P}_m(\mathbf{r}_0)\Delta_r\Delta_r^T\mathbf{P}_m^\perp(\mathbf{r}_0) + 2\mathbf{P}_m^\perp(\mathbf{r}_0)\Delta_r\Delta_r^T\mathbf{P}_m(\mathbf{r}_0) \\ & + (\Delta_r^T\mathbf{P}_m(\mathbf{r}_0)\Delta_r)\mathbf{P}_m^\perp(\mathbf{r}_0) + 2(\Delta_r^T\mathbf{P}_m^\perp(\mathbf{r}_0)\Delta_r)\mathbf{P}_m(\mathbf{r}_0) \\ \Xi_{2,0} = & 2\mathbf{P}_m(\mathbf{r}_0)\Delta_r\Delta_r^T\mathbf{P}_m^\perp(\mathbf{r}_0) + 2\mathbf{P}_m^\perp(\mathbf{r}_0)\Delta_r\Delta_r^T\mathbf{P}_m(\mathbf{r}_0) \\ & - (\Delta_r^T\mathbf{P}_m^\perp(\mathbf{r}_0)\Delta_r)\mathbf{P}_m^\perp(\mathbf{r}_0) \\ \Xi_{3,0} = & (\Delta_r^T\mathbf{P}_m(\mathbf{r}_0)\Delta_r)\mathbf{P}_m^\perp(\mathbf{r}_0). \end{aligned}$$

Finally, the spectral norm of the reminder term $\mathcal{R}_m(\bar{\mathbf{r}}, \Delta_r)$ can be upper bounded as

$$\|\mathcal{R}_m(\bar{\mathbf{r}}, \Delta_r)\| \leq P\left(\|\bar{\mathbf{r}} - \mathbf{p}_m\|^{-1}\right) \|\Delta_r\|^3$$

where $P(\cdot)$ is a nice polynomial (cf. definition in Remark 1).

Proof. See Appendix A. \square

Based on the above result and mimicking the construction of the channel matrix $\mathbf{H}_{\text{pol}}(\mathbf{r})$ in (1) from the individual $\mathbf{H}_m(\mathbf{r})$, we can more compactly write

$$\mathbf{H}_{\text{pol}}(\mathbf{r}) = \mathbf{H}_{\text{pol}}(\mathbf{r}_0) + \mathcal{G}_{\text{pol}}(\Delta_r) + \mathcal{H}_{\text{pol}}(\Delta_r) + \mathcal{R}_{\text{pol}}(\bar{\mathbf{r}}, \Delta_r) \quad (6)$$

where $\mathcal{G}_{\text{pol}}(\Delta_r)$, $\mathcal{H}_{\text{pol}}(\Delta_r)$ and $\mathcal{R}_{\text{pol}}(\bar{\mathbf{r}}, \Delta_r)$ have dimensions $r_{\text{pol}} \times (2M+1) t_{\text{pol}}$ and are built from the corresponding quantities in Proposition 1 in the same way as (1). Using (6) in (3) we can obtain the following interesting result.

Corollary 1. The SNR in (3) accepts the expansion

$$\text{SNR}(\mathbf{r}) = \text{SNR}(\mathbf{r}_0) + \frac{\bar{P}}{\sigma^2} \frac{\mathbf{w}^H(*)\mathbf{w}}{2M+1} + \epsilon_M \quad (7)$$

where

$$(*) = \mathcal{G}_{\text{pol}}^H(\Delta_r)\mathbf{H}_{\text{pol}}(\mathbf{r}_0) + \mathbf{H}_{\text{pol}}^H(\mathbf{r}_0)\mathcal{G}_{\text{pol}}(\Delta_r) \quad (8)$$

$$+ \mathcal{H}_{\text{pol}}^H(\Delta_r)\mathbf{H}_{\text{pol}}(\mathbf{r}_0) + \mathbf{H}_{\text{pol}}^H(\mathbf{r}_0)\mathcal{H}_{\text{pol}}(\Delta_r) \quad (9)$$

$$+ \mathcal{G}_{\text{pol}}^H(\Delta_r)\mathcal{G}_{\text{pol}}(\Delta_r) \quad (10)$$

and where ϵ_M is a third-order error term and is such that $|\epsilon_M| \leq K \|\Delta_r\|^3$ for a certain nice constant K .

Proof. See Appendix B. \square

We recall that \mathbf{w} is chosen to be the left singular vector associated to the maximum singular value of the channel matrix $\mathbf{H}_{\text{pol}}(\mathbf{r}_0)$. This implies that \mathbf{w} alternatively expressed as³

$$\mathbf{w} = \frac{1}{\sqrt{2M+1}\sqrt{\lambda_{\max}}} \mathbf{H}_{\text{pol}}^H(\mathbf{r}_0) \mathbf{u} \quad (11)$$

³To see this, simply use the SVD formula $\mathbf{H}_{\text{pol}}^H(\mathbf{r}_0) = \sqrt{2M+1}\mathbf{V}\Sigma^{1/2}\mathbf{U}^H$.

where we recall that \mathbf{u} is the eigenvector associated to the maximum eigenvalue of $\mathbf{H}_{\text{pol}}(\mathbf{r}_0)\mathbf{H}_{\text{pol}}^H(\mathbf{r}_0)/(2M+1)$, denoted as λ_{max} . By inserting (11) into the expression of $\text{SNR}(\mathbf{r})$ in (7) we see that the expression can be reformulated as

$$\text{SNR}(\mathbf{r}) = \text{SNR}(\mathbf{r}_0) + \frac{\bar{P}}{\sigma^2} \mathbf{u}^H(\star) \mathbf{u} + \epsilon_M \quad (12)$$

where now

$$\begin{aligned} (\star) &= \frac{\mathbf{H}_{\text{pol}}(\mathbf{r}_0) \mathcal{G}_{\text{pol}}^H(\Delta_r) + \mathcal{G}_{\text{pol}}(\Delta_r) \mathbf{H}_{\text{pol}}^H(\mathbf{r}_0)}{2M+1} \\ &+ \frac{\mathbf{H}_{\text{pol}}(\mathbf{r}_0) \mathcal{H}_{\text{pol}}^H(\Delta_r) + \mathcal{H}_{\text{pol}}(\Delta_r) \mathbf{H}_{\text{pol}}^H(\mathbf{r}_0)}{2M+1} \\ &+ \frac{\mathbf{H}_{\text{pol}}(\mathbf{r}_0) \mathcal{G}_{\text{pol}}^H(\Delta_r) \mathcal{G}_{\text{pol}}(\Delta_r) \mathbf{H}_{\text{pol}}^H(\mathbf{r}_0)}{\lambda_{\text{max}}(2M+1)^2}. \end{aligned}$$

Hence, we can investigate the behavior of $\text{SNR}(\mathbf{r})$ around $\text{SNR}(\mathbf{r}_0)$ by simply studying the two matrices $\mathcal{G}_{\text{pol}}(\Delta_r)\mathbf{H}_{\text{pol}}^H(\mathbf{r}_0)/(2M+1)$ and $\mathcal{H}_{\text{pol}}(\Delta_r)\mathbf{H}_{\text{pol}}^H(\mathbf{r}_0)/(2M+1)$. These two matrices have a complicated analytical form, but we can significantly simplify the result by assuming that the intended receiver is located on the yz -plane, i.e. $x_0 = 0$. In order to present the results, we introduce the following key quantities

$$\begin{aligned} s_M^{(k)} &= \frac{1}{2M+1} \sum_{m=-M}^M \frac{1}{\|\mathbf{r}_0 - \mathbf{p}_m\|^k} \\ \bar{s}_M^{(k)} &= \frac{1}{2M+1} \sum_{m=-M}^M \frac{m\Delta_T - y_0}{\|\mathbf{r}_0 - \mathbf{p}_m\|^{k+1}} \end{aligned}$$

where $k \in \mathbb{N}$.

Proposition 2. *When $x_0 = 0$ (intended receiver on the yz -plane), the identity in (12) particularizes to*

$$\text{SNR}(\mathbf{r}) = \text{SNR}(\mathbf{r}_0) [1 - (2\Delta_r^T \mathbf{m}_M + \Delta_r^T \mathcal{M}_M \Delta_r)] + \epsilon_M \quad (13)$$

where the column vector \mathbf{m}_M and the matrix \mathcal{M}_M are defined as follows. The column vector \mathbf{m}_M only has non-zero entries in the second and third position, so that we can write $\mathbf{m}_M = [0, (\mathbf{m}_M^{(2)})^T]^T$ where

$$\mathbf{m}_M^{(2)} = \frac{1}{s_M^{(2)}} \begin{bmatrix} -\bar{s}_M^{(3)} & z_0 s_M^{(4)} \end{bmatrix}^T.$$

Regarding \mathcal{M}_M , it is a block-diagonal matrix with diagonals given by a scalar $\gamma_M^{(1)}$ and a 2×2 real-valued matrix $\mathcal{M}_M^{(2)}$, that is

$$\mathcal{M}_M = \begin{bmatrix} \gamma_M^{(1)} & \mathbf{0} \\ \mathbf{0} & \mathcal{M}_M^{(2)} \end{bmatrix}. \quad (14)$$

The scalar entry takes the form

$$\gamma_M^{(1)} = \frac{1}{(s_M^{(2)})^2} \left[3s_M^{(2)}s_M^{(4)} - (s_M^{(3)})^2 - z_0^2 (s_M^{(4)})^2 \right] \quad (15)$$

and is always non-negative, i.e. $\gamma_M^{(1)} \geq 0$. As for the 2×2 matrix $\mathcal{M}_M^{(2)}$, it can be written as $\mathcal{M}_M^{(2)} = \mathcal{A}_M + (2\pi/\lambda)^2 \mathcal{B}_M$ with \mathcal{A}_M and \mathcal{B}_M being respectively defined as in (16)-(17) at the top of the next page.

Proof. See Appendix C. \square

If we disregard the high order error terms, which decay as $O(\|\Delta_r\|^3)$, the set of points for which the $\text{SNR}(\mathbf{r}) = \kappa \text{SNR}(\mathbf{r}_0)$ where $\kappa \in (0, 1)$ is asymptotically described by the equation

$$1 - \kappa = 2\Delta_r^T \mathbf{m}_M + \Delta_r^T \mathcal{M}_M \Delta_r \quad (18)$$

or alternatively as

$$\begin{bmatrix} \Delta_r & 1 \end{bmatrix} \begin{bmatrix} \mathcal{M}_M & \mathbf{m}_M \\ \mathbf{m}_M^T & -(1-\kappa) \end{bmatrix} \begin{bmatrix} \Delta_r \\ 1 \end{bmatrix} = 0$$

which is the equation of a quadric surface [32]. Disregarding all degenerated situations, this quadric surface can either be an ellipsoid or a hyperboloid (of one or two sheets). The beamfocusing feasibility region will therefore be associated to the region of points in space for which this quadric is an ellipsoid, which is the only case where the enclosed region has with finite volume. This situation occurs if and only if the three eigenvalues of \mathcal{M}_M are positive.

Given the structure of \mathbf{m}_M and \mathcal{M}_M , we see that the ellipsoid will always be symmetric with respect to the yz -plane (where the receiver is assumed to be located). The length of the three semi-axes, which we denote as $l_M^{(1)}(\mathbf{r}_0)$ (along the x -axis), $l_M^{(2)}(\mathbf{r}_0)$ and $l_M^{(3)}(\mathbf{r}_0)$ (on the yz -plane) can be expressed in closed form. Indeed, if we denote as $\gamma_M^{(1)} \geq \gamma_M^{(2)} \geq \gamma_M^{(3)} > 0$ the three eigenvalues of \mathcal{M} (so that $\gamma_M^{(1)}$ is as defined in (15) and $\gamma_M^{(2)}, \gamma_M^{(3)}$ are the eigenvalues of $\mathcal{M}_M^{(2)}$), we can express

$$l_M^{(k)}(\mathbf{r}_0) = \sqrt{\frac{\mu_M}{\gamma_M^{(k)}}} \quad (19)$$

where

$$\begin{aligned} \mu_M &= \frac{-1}{\det \mathcal{M}_M} \det \begin{bmatrix} \mathcal{M}_M & \mathbf{m}_M \\ \mathbf{m}_M^T & \kappa - 1 \end{bmatrix} \\ &= 1 - \kappa + (\mathbf{m}_M^{(2)})^T (\mathcal{M}_M^{(2)})^{-1} \mathbf{m}_M^{(2)}. \end{aligned}$$

In particular, the volume enclosed by the ellipsoid where the achieved SNR is at least $\kappa \text{SNR}(\mathbf{r}_0)$ can be expressed as

$$\mathcal{V}_M(\mathbf{r}_0) = \frac{4\pi}{3} l_M^{(1)}(\mathbf{r}_0) l_M^{(2)}(\mathbf{r}_0) l_M^{(3)}(\mathbf{r}_0) = \frac{4\pi}{3} \sqrt{\frac{\mu_M^3}{\gamma_M^{(1)} \gamma_M^{(2)} \gamma_M^{(3)}}}$$

which effectively goes to infinity as $\mathcal{M}_M^{(2)}$ becomes singular. The center of the ellipsoid is located at the point $\mathbf{r}_0 - \mathcal{M}_M^{-1} \mathbf{m}_M$ of the three dimensional space (equivalently at the point $[y_0, z_0]^T - (\mathcal{M}_M^{(2)})^{-1} \mathbf{m}_M^{(2)}$ of the yz -plane).

All these parameters allows us to establish the beamfocusing feasibility region (that is the region where the quadric is an ellipsoid) and the local effectiveness of beamfocusing operation (given by the volume of the corresponding ellipsoid for any fixed κ). From the analytical perspective, though, it is difficult to gain much insight from the above expressions, since the different terms need to be evaluated for each fixed M and Δ_T . In the next section we consider the holographic regime whereby the number of elements of the ULA increases to infinity ($M \rightarrow \infty$) while the distance between consecutive elements converges to zero at the same rate ($\Delta_T \rightarrow 0$)

$$\mathcal{A}_M = \frac{1}{\left(s_M^{(2)}\right)^2} \begin{bmatrix} \left(3z_0^2 s_M^{(6)} - 2s_M^{(4)}\right) s_M^{(2)} - \left(\bar{s}_M^{(3)}\right)^2 & \left(s_M^{(4)} \bar{s}_M^{(3)} + 3s_M^{(2)} \bar{s}_M^{(5)}\right) z_0 \\ \left(s_M^{(4)} \bar{s}_M^{(3)} + 3\bar{s}_M^{(5)} s_M^{(2)}\right) z_0 & \left(s_M^{(4)} - 3s_M^{(6)} z_0^2\right) s_M^{(2)} - \left(s_M^{(4)} z_0\right)^2 \end{bmatrix} \quad (16)$$

$$\mathcal{B}_M = \frac{1}{\left(s_M^{(2)}\right)^2} \begin{bmatrix} \left(s_M^{(2)}\right)^2 - z_0^2 s_M^{(2)} s_M^{(4)} - \left(\bar{s}_M^{(2)}\right)^2 & \left(\bar{s}_M^{(2)} s_M^{(3)} - \bar{s}_M^{(3)} s_M^{(2)}\right) z_0 \\ \left(s_M^{(3)} \bar{s}_M^{(2)} - \bar{s}_M^{(3)} s_M^{(2)}\right) z_0 & z_0^2 \left(s_M^{(4)} s_M^{(2)} - \left(s_M^{(3)}\right)^2\right) \end{bmatrix} \quad (17)$$

so that the total dimension of the aperture converges to $(2M+1)\Delta_T \rightarrow 2L > 0$. It can be seen that the approximation is quite accurate even in situations where the interelement separation is relatively high, as will be shown in the numerical evaluation study below.

III. THE HOLOGRAPHIC REGIME

The above analysis can be simplified by considering the holographic regime, according to which we allow $M \rightarrow \infty$ and $\Delta_T \rightarrow 0$ so that $M\Delta_T \rightarrow L$, $0 < L < \infty$. In these circumstances, one can easily see that $s_M^{(k)} \rightarrow \chi_k$ and $\bar{s}_M^{(k)} \rightarrow \bar{\chi}_k$, where the quantities χ_k and $\bar{\chi}_k$ are defined as follows. On the one hand, for $k \in \mathbb{N}$ the quantities $\bar{\chi}_k$ are given by

$$\bar{\chi}_k = \frac{1}{2L(k-1)} \left[\left((L+y_0)^2 + z_0^2 \right)^{-(k-1)/2} - \left((L-y_0)^2 + z_0^2 \right)^{-(k-1)/2} \right]$$

On the other hand, the quantities χ_k for $k = 2, 3, 4, 6$ are defined as [31]:

$$\begin{aligned} \chi_2 &= \frac{1}{2Lz_0} \left[\arctan \frac{L-y_0}{z_0} + \arctan \frac{L+y_0}{z_0} \right] \\ \chi_3 &= \frac{1}{2Lz_0^2} \left[\frac{L-y_0}{\sqrt{(L-y_0)^2 + z_0^2}} + \frac{L+y_0}{\sqrt{(L+y_0)^2 + z_0^2}} \right] \\ \chi_4 &= \frac{1}{4Lz_0^2} \left[\frac{L-y_0}{(L-y_0)^2 + z_0^2} + \frac{L+y_0}{(L+y_0)^2 + z_0^2} \right] + \frac{\chi_2}{2z_0^2} \\ \chi_6 &= -\frac{1}{8Lz_0^4} \left[\frac{(L-y_0)^3}{\left((L-y_0)^2 + z_0^2 \right)^2} + \frac{(L+y_0)^3}{\left((L+y_0)^2 + z_0^2 \right)^2} \right] \\ &\quad + \frac{5\chi_4}{4z_0^2} - \frac{\chi_2}{4z_0^4}. \end{aligned}$$

This implies that \mathbf{m}_M in Proposition 2 will converge to \mathbf{m} given by $\mathbf{m} = [0, \mathbf{m}_2]^T$ where

$$\mathbf{m}_2 = \frac{1}{\chi_2} \begin{bmatrix} -\bar{\chi}_3 \\ \chi_4 z_0 \end{bmatrix}. \quad (20)$$

On the other hand, $\gamma_M^{(1)}$ will converge to

$$\gamma_1 = \frac{3\chi_2\chi_4 - \bar{\chi}_3^2 - z_0^2\chi_4^2}{\chi_2^2} \quad (21)$$

and $\mathcal{M}_M^{(2)}$ will converge to \mathcal{M}_2 given by

$$\begin{aligned} \mathcal{M}_2 &= \quad (22) \\ &\frac{1}{\chi_2^2} \begin{bmatrix} (3\chi_6 z_0^2 - 2\chi_4)\chi_2 - \bar{\chi}_3^2 & (3\chi_2\bar{\chi}_5 + \chi_4\bar{\chi}_3) z_0 \\ (3\chi_2\bar{\chi}_5 + \chi_4\bar{\chi}_3) z_0 & \chi_2\chi_4 - z_0^2(\chi_4^2 + 3\chi_2\chi_6) \end{bmatrix} \\ &+ \left(\frac{2\pi}{\lambda}\right)^2 \frac{1}{\chi_2^2} \begin{bmatrix} \chi_2^2 - z_0^2\chi_2\chi_4 - \bar{\chi}_3^2 & (\bar{\chi}_2\chi_3 - \chi_2\bar{\chi}_3) z_0 \\ (\bar{\chi}_2\chi_3 - \chi_2\bar{\chi}_3) z_0 & (\chi_2\chi_4 - \chi_3^2) z_0^2 \end{bmatrix}. \end{aligned}$$

The first term on the right hand side of (13) will also converge in the holographic regime to a quantity obtained by replacing \mathbf{m}_M and \mathcal{M}_M with \mathbf{m} and \mathcal{M} respectively. Observe also that, since $|\epsilon_M| \leq K \|\Delta_r\|^3$ for a certain nice constant K , we will also have $\limsup_{M \rightarrow \infty} |\epsilon_M| \leq K \|\Delta_r\|^3$ and the error term will also be of order $O(\|\Delta_r\|^3)$ in the holographic regime.

Noting that $\gamma_1 > 0$ one can conclude that the region where beamfocusing is feasible can be identified with the region of space where the two eigenvalues of \mathcal{M}_2 are positive, i.e. $\mathcal{M}_2 > 0$. Here again, this corresponds to the corresponding quadric surface being an ellipsoid symmetric with respect to the yz -plane. The three semiaxes of the ellipsoid will now be given by the limits of $l_M^{(k)}$, $k = 1, 2, 3$, in (19). In other words, we will have $l_M^{(k)} \rightarrow l_k = \sqrt{\mu/\gamma_k}$ where γ_k , $k = 1, 2, 3$, are the eigenvalues of \mathcal{M} and where $\mu = 1 - \kappa + \mathbf{m}_2^T \mathcal{M}_2^{-1} \mathbf{m}_2$ with \mathbf{m}_2 and \mathcal{M}_2 as defined in (20)-(22). The ellipsoid itself will be centered at the point $[y_0, z_0]^T - \mathcal{M}_2^{-1} \mathbf{m}_2$ of the yz -plane.

Remark 2. It can be seen that $D^k \chi_k$ and $D^k \bar{\chi}_k$ are functions of $\varrho = L/D$ and θ and no other variable, where we recall that θ denotes the elevation angle of the intended receiver and D is the distance between the intended receiver and the center of the ULA (see Fig. 1). This implies that $D^2 \gamma_1$ and $D \mathbf{m}_2$ are also a function of ϱ and θ only, whereas $D^2 \mathcal{M}_2$ can be expressed as a function of ϱ , θ and L/λ . In particular, we observe that the eigenvalues of $D^2 \mathcal{M}_2$ are also functions of these three variables only. We can therefore establish the region where beamfocusing is possible as the region where the three eigenvalues of this matrix are positive, which can easily be evaluated for any fixed value of L/λ .

Indeed, by considering a range of values of the elevation θ in the set $(-\pi/2, \pi/2)$ (see Fig. 1), one can evaluate the minimum eigenvalue of $D^2 \mathcal{M}_2$ as a function of ϱ and establish the values of this quantity for which the minimum eigenvalue is positive. The region where beamfocusing is feasible will easily be established for each value of L/λ under consideration. This is illustrated in Fig. 2, where we represent the beamfocusing feasibility regions for different values of this parameter. The boundary of the feasibility region is numerically obtained by evaluating the minimum eigenvalue

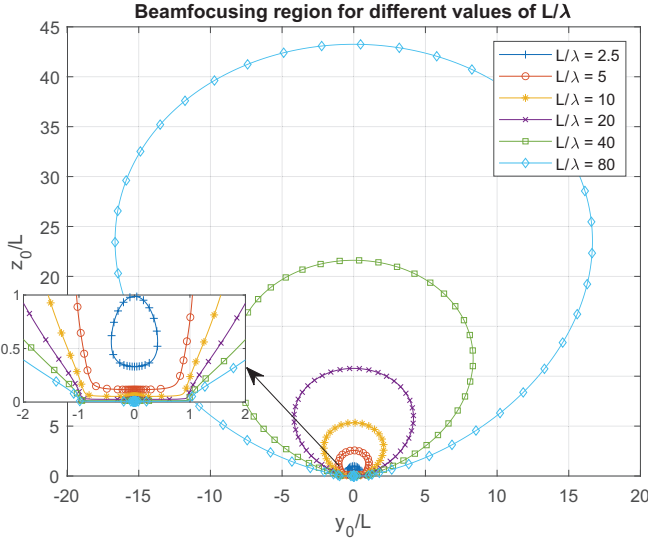


Fig. 2. Spatial regions where beamfocusing is feasible for different values of the array size relative to the wavelength in the holographic regime (L/λ).

of $D^2\mathcal{M}_2$ as a function of $\varrho = L/D$ and finding the values of ϱ where this eigenvalue becomes zero. In general terms, it can be observed that depending on the value of the elevation θ , the feasibility region is either empty or consists of a single interval of values in ϱ .

The quotient between the semiaxes of the ellipsoid and the distance D (that is l_k/D) will also be a function of ϱ , θ and L/λ only. Furthermore, if we denote by $\mathcal{V}(\mathbf{r}_0)$ the volume of the ellipsoid in the holographic regime, that is

$$\mathcal{V}(\mathbf{r}_0) = \frac{4\pi}{3} l_1 l_2 l_3 = \frac{4\pi}{3} \sqrt{\frac{\mu^3}{\gamma_1 \gamma_2 \gamma_3}}$$

we have that $\mathcal{V}(\mathbf{r}_0)/D^3$ is a function of ϱ , θ and L/λ only. This quantity provides a quantitative measure of the efficiency of beamfocusing within the feasibility region, see further Fig.3.

The above description in the holographic regime provides an analytical framework independent of M that can be used to establish the regions of beamfocusing and the corresponding κ -efficiency as a function of position of the intended receiver. In the following two subsections, we try to provide some more insight by focusing on two special cases. We will first consider the case where the intended receiver is located at the broadside of the array, so that $y_0 = 0$. Next, we will provide an approximation of the above quantities for reasonably high values of D/L , where we recall that $D = \sqrt{y_0^2 + z_0^2}$ is the distance between the intended receiver and the center of the ULA and L is the one-sided dimension of the aperture.

A. Case $y_0 = 0$ (intended receiver on the broadside)

When $y_0 = 0$ we can simplify the above expressions by noting that $\bar{\chi}_k = 0$ for all k , whereas $\chi_2 = (Lz_0)^{-1} \arctan(L/z_0)$ and similar simplifications are obtained for χ_3, χ_4, χ_6 . From this, we find that γ_1 particularizes to

$$\gamma_1 = \frac{1}{4z_0^2\chi_2^2} \left(5\chi_2 - \frac{1}{(L^2 + z_0^2)} \right) \left(\chi_2 + \frac{1}{(L^2 + z_0^2)} \right).$$

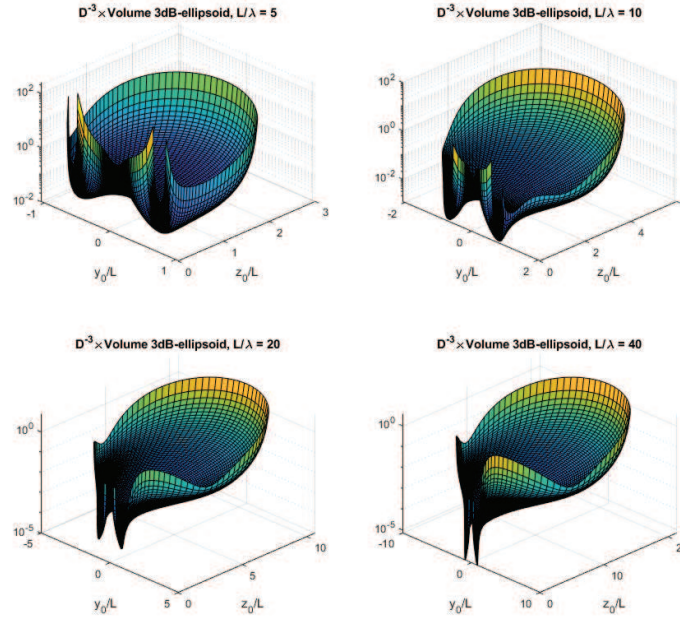


Fig. 3. Volume of the asymptotical ellipsoid that characterizes the 3dB loss with respect to the maximum SNR ($\kappa = 0.5$) for different values of L/λ .

On the other hand, \mathcal{M}_2 becomes diagonal, with diagonal entries that we will denote γ_2, γ_3 given by

$$\begin{aligned} \gamma_2 &= \frac{1}{8\chi_2 z_0^2} \left(\frac{L^2 + 7z_0^2}{(L^2 + z_0^2)^2} + \chi_2 \right) \\ &\quad + \frac{1}{2} \left(\frac{2\pi}{\lambda} \right)^2 \left(1 - \frac{1}{\chi_2 (L^2 + z_0^2)} \right) \\ \gamma_3 &= -\frac{1}{\chi_2^2} \frac{1}{8z_0^2} \left(7\chi_2^2 + 3 \frac{3L^2 + 5z_0^2}{(L^2 + z_0^2)^2} \chi_2 + \frac{2}{(L^2 + z_0^2)^2} \right) \\ &\quad + \left(\frac{2\pi}{\lambda} \right)^2 \frac{1}{2\chi_2^2} \left(\chi_2^2 + \frac{\chi_2}{(L^2 + z_0^2)} - \frac{1}{z_0^2} \frac{2}{(L^2 + z_0^2)} \right). \end{aligned}$$

The first two eigenvalues of \mathcal{M} (i.e. γ_1, γ_2) are positive, since

$$\chi_2 (L^2 + z_0^2) = \left(1 + \frac{z_0^2}{L^2} \right) \frac{L}{z_0} \arctan \frac{L}{z_0} > 1$$

so that beamfocusing will be feasible whenever $\gamma_3 > 0$. Defining $\varphi_2(\varrho) = \varrho^{-1} \arctan \varrho$ where $\varrho = L/D$, one can characterize the beamfocusing feasibility segment as the set of points for which $\gamma_3 > 0$, a condition that can be expressed as

$$\frac{\varrho}{2\pi} \sqrt{\frac{7(1 + \varrho^2)^2 \varphi_2^2(\varrho) + 3(5 + 3\varrho^2) \varphi_2(\varrho) + 2}{4(1 + \varrho^2)(\varphi_2^2(\varrho)(1 + \varrho^2) + \varphi_2(\varrho) - 2)}} \leq \frac{L}{\lambda}. \quad (23)$$

The left hand side is a continuous function of $\varrho = L/D$ that presents a single inflection point (local minima) at $\varrho = 1.72776$ where it takes the value 2.2048. This is illustrated in Fig. 4, where we represent the left hand side of (23) as a function of $\varrho^{-1} = D/L$. The region of feasibility of beamfocusing can be described as the region between the two roots of (23), which can be obtained by considering the intersection of the blue solid line in Fig. 4 with a horizontal line at L/λ . The

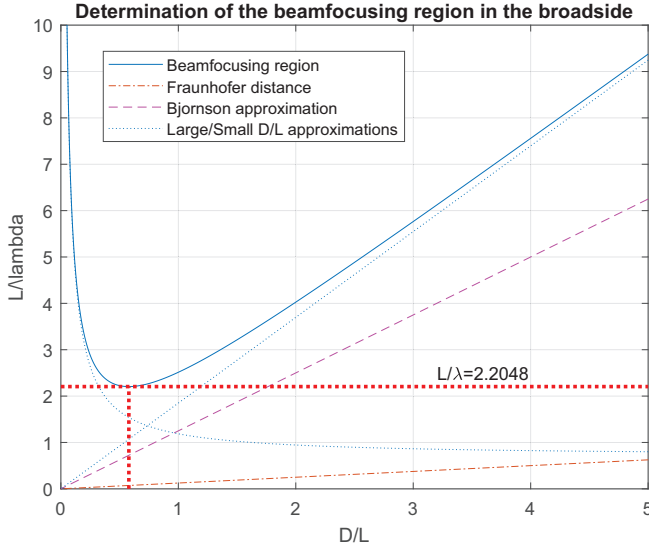


Fig. 4. Representation of the function on the left hand side of (23) as a function of $\varrho^{-1} = D/L$. The feasibility segment for beamfocusing on the broadside is obtained by selecting the interval where this curve is lower than L/λ . Additionally, we represent the two lines that determine the Fraunhofer distance by the same procedure (red dash-dotted line) as well as the beamfocusing radius approximation in [33, Theorem 1], consisting of one tenth of the Fraunhofer distance (magenta dashed line).

inflection point implies that beamfocusing along the broadside of the array is only possible when $L > 2.2048\lambda$. We can gain some insight into the beamfocusing feasibility region by considering a large/small- ϱ approximation of the left hand side of (23). Indeed, for large values of ϱ the left hand side of (23) can be expanded as

$$\frac{3\sqrt{15}}{2\pi\varrho} + o(1)$$

whereas for small values of ϱ it can be approximated as

$$\frac{1}{4}\sqrt{\frac{7}{\pi^2 - 8}} \left(\varrho + \frac{\pi^2 + 20}{14\pi(\pi^2 - 8)} \right) + o(1).$$

These two approximations are shown in Fig. 4 in blue dotted lines. Using these approximations, we can establish that for large values of D/L , the maximum distance that guarantees the feasibility of beamfocusing can be approximated as $D_{\max} \approx 2\pi L^2 / (3\lambda\sqrt{15}) = \pi / (12\sqrt{15}) D_{\text{Fraun}}$, where $D_{\text{Fraun}} = 8L^2/\lambda$ is the Fraunhofer distance. For small values of D/L the minimum distance can be approximated as

$$D_{\min} \approx L \left(\frac{4L}{\lambda} \sqrt{\frac{\pi^2 - 8}{7}} - \frac{\pi^2 + 20}{14\pi(\pi^2 - 8)} \right)^{-1}$$

which becomes proportional to λ for large apertures. This is quite often within the reactive region of the electromagnetic field (i.e. below the Fresnel distance).

B. Approximation for high D/L

We now turn to the more interesting case where the receiver is not necessarily located in the broadside of the array, so that the angle θ in Fig. 1 can take any value in the set $(-\pi/2, \pi/2)$.

In particular, we will try to gain some insights into the beamfocusing achievability region and the actual shape of the corresponding achievability ellipses when the distance D is large compared to the ULA aperture side length L .

As pointed out in Remark 2, both $D^k \chi_k$ and $D^k \bar{\chi}_k$ can be expressed as analytic functions of $\varrho = L/D$ and θ only. In particular, in order to gain some further insight into the behavior of the above description, one can consider the Taylor series approximation of all these functions around $\varrho = 0$. The Taylor series of $D^k \chi_k$ for $k = 2, 4, 6$ and $D^k \bar{\chi}_k$ for $k = 5$ around $\varrho = L/D = 0$ were presented in [34, Appendix A]. Similarly, one can see that

$$\begin{aligned} D^3 \chi_3 &= 1 + (2 - 5/2 \cos^2 \theta) \varrho^2 + O(\varrho^4) \\ D^2 \bar{\chi}_2 &= -\sin \theta [1 + (1 - 5/2 \cos^2 \theta) \varrho^2] + O(\varrho^4) \\ D^3 \bar{\chi}_3 &= -\sin \theta [1 + (2 - 4 \cos^2 \theta) \varrho^2] + O(\varrho^4). \end{aligned}$$

A direct application of these series in (21) shows that

$$\begin{aligned} D^2 \gamma_1 &= \frac{(5 \cos^2 \theta - 1)(\cos^2 \theta + 1)}{4 \cos^6 \theta} \\ &+ \frac{(2 \cos^2 \theta - 1)(4 \cos^4 \theta - 3 \cos^2 \theta - 3)}{6 \cos^8 \theta} \varrho^2 + O(\varrho^4). \end{aligned}$$

Regarding the matrix \mathcal{M}_2 , it can be expanded as in (24) at the top of the next page, where we have used the short-hand notation $c_\theta = \cos \theta$ and $s_\theta = \sin \theta$. The two eigenvalues of this matrix can in turn be asymptotically expressed as

$$\begin{aligned} D^2 \gamma_2 &= 1 + \frac{c_\theta^2}{3} \left(\frac{2\pi L}{\lambda} \right)^2 + \\ &+ \left[\frac{7 - 11c_\theta^2}{3} + \left(\frac{2\pi L}{\lambda} \right)^2 \frac{30 - 43c_\theta^2}{45} c_\theta^2 \right] \varrho^2 + O(\varrho^4) \\ D^2 \gamma_3 &= -3 + \left[\frac{-20 + 27c_\theta^2}{3} + \left(\frac{2\pi L}{\lambda} \right)^2 \frac{c_\theta^4}{45} \right] \varrho^2 + O(\varrho^4). \end{aligned}$$

If we disregard the terms of order $O(\varrho^4)$ in the above expansion for $D^2 \gamma_3$, we can approximate the feasibility region of beamfocusing ($\gamma_3 > 0$) as the set of points such that

$$\left(\frac{D}{L} \right)^2 < \frac{1}{9} \left[-20 + 27 \cos^2 \theta + \frac{\cos^4 \theta}{15} \left(\frac{2\pi L}{\lambda} \right)^2 \right]. \quad (25)$$

Fig. 5 shows a comparison between the actual beamfocusing feasibility region in the holographic regime (blue solid lines) and the asymptotic approximation in (25) (red dashed lines) for different values of L/λ . It can be seen that the approximation is quite accurate for $L/\lambda \geq 10$, that is when the total dimension of the ULA is at least 20λ , which corresponds to the situation where the feasibility region is sufficiently large in terms of D/L .

Finally, we can characterize the behavior for large D/L of the three semiaxes of the corresponding ellipsoid. To see that, we can first find an expansion Dm_2 as a function of $\varrho = L/D$, namely

$$Dm_2 = \left[\begin{array}{c} \sin \theta \left[1 + \left(\frac{1 - \frac{8}{3} \cos^2 \theta}{7} \right) \varrho^2 \right] \\ \cos \theta \left[1 + \left(\frac{7 - \frac{8}{3} \cos^2 \theta}{3} \right) \varrho^2 \right] \end{array} \right] + O(\varrho^4).$$

$$\begin{aligned}
D^2\mathcal{M}_2 = & \begin{bmatrix} -3 + 4c_\theta^2 & -4s_\theta c_\theta \\ -4s_\theta c_\theta & 1 - 4c_\theta^2 \end{bmatrix} + \left(\frac{2\pi L}{\lambda}\right)^2 \frac{c_\theta^2}{3} \begin{bmatrix} c_\theta^2 & -s_\theta c_\theta \\ -s_\theta c_\theta & s_\theta^2 \end{bmatrix} \\
+ \frac{1}{3} & \begin{bmatrix} -20 + 92c_\theta^2 - 76c_\theta^4 & -s_\theta c_\theta (46 - 76c_\theta^2) \\ -s_\theta c_\theta (46 - 76c_\theta^2) & 7 - 76c_\theta^2 + 76c_\theta^4 \end{bmatrix} \varrho^2 + \left(\frac{2\pi L}{\lambda}\right)^2 \frac{c_\theta^2}{45} \begin{bmatrix} c_\theta^2 (61 - 74c_\theta^2) & -s_\theta c_\theta (45 - 74c_\theta^2) \\ -s_\theta c_\theta (45 - 74c_\theta^2) & 30 - 103c_\theta^2 + 74c_\theta^4 \end{bmatrix} \varrho^2 + O(\varrho^4)
\end{aligned} \tag{24}$$

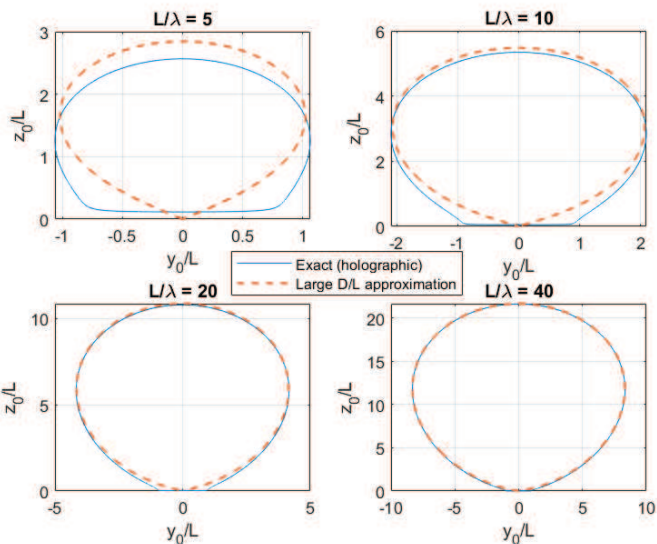


Fig. 5. Comparison of the actual feasibility region for beamfocusing and the large D/L approximation for different values of L/λ .

Using this and the expression of $D^2\mathcal{M}_2$ above one can obtain

$$\mu = \left(\frac{2}{3} - \kappa\right) - \frac{1}{135} \left(15c_\theta^2 - 10 + \frac{c_\theta^4}{3} \left(\frac{2\pi L}{\lambda}\right)^2\right) \varrho^2 + O(\varrho^4).$$

From this, one can obtain the corresponding expansion of the three semi-axes of the ellipsoid, which can be used to describe the spatial efficiency of the beamfocusing mechanism.

IV. NUMERICAL ANALYSIS

In this section we provide a numerical study of the accuracy of the above asymptotic approximations in a practical setting. In order to justify the holographic approximations, we consider a rather standard situation where the ULA elements are separated by $\Delta_T = \lambda/2$. The transmit array consisted of $2M+1 = 101$ antennas, so that the total dimension of the array was $2L = 25\lambda$. To generate the actual channel, we assumed a frequency of operation of 3 GHz, which corresponds to a wavelength equal to 0.1 m. Fig. 6 to Fig. 8 represent the region of the yz -plane that achieves a SNR that is at least 3 dB below the optimum one for different positions of the intended receiver (represented as markers). Apart from the actual region (represented in solid blue lines), we also plot the corresponding conic curves that are obtained by intersecting the corresponding quadric achievability surfaces with the yz -plane. More specifically, red dotted lines represent the achievability regions obtained by using the finite- M approximation

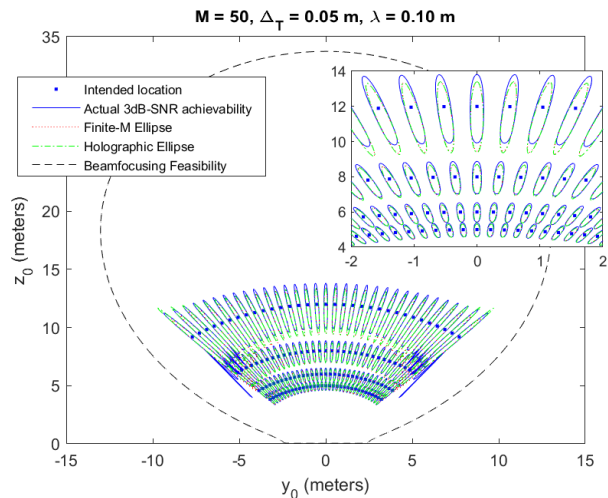


Fig. 6. Representation of the region that achieves an SNR at least 3dB below the optimum ($\kappa = 0.5$): true region (blue solid lines), finite- M second order approximation (red dotted lines) and holographic approximation (green dash-dotted lines) for different intended locations (markers).

in Proposition 2, whereas green dash-dotted lines represent the corresponding holographic representation obtained as $M \rightarrow \infty$ and $\Delta_T \rightarrow 0$ while $M\Delta_T \rightarrow L$, as presented in Section III. We also represent, in black dash-dotted line, the holographic approximation to the beamfocusing achievability region.

Fig. 6 considers the situation where the intended receivers are relatively close to the transmit array. In this situation, the true 3-dB SNR achievability regions are very well approximated by ellipses. Furthermore, both the finite- M conic as its holographic approximation are quite close to the actual achievability region. The situation is somewhat different in Fig. 7, which represents a situation where the intended receivers are further away from the ULA and closer to the holographic boundary of the region of beamfocusing feasibility (black dashed line). In this case, we observe that the actual 3-dB SNR achievability regions (blue solid lines) are more complicated than just mere ellipses⁴. However, they are still well-focused regions that are reasonably well approximated by ellipses near the intended receiver. Finally, Fig. 8 represents the situation where the intended receivers are located outside the holographic region for beamfocusing feasibility (black dashed lines). In this case, the actual 3-dB SNR achievability regions are well approximated by hyperbolas and the ULA does no longer exhibit beamfocusing capabilities. In all the situations we can see that holographic approximations are

⁴Obviously, the shape of the achievability region becomes much closer to an ellipse if we consider higher values of κ in (18).

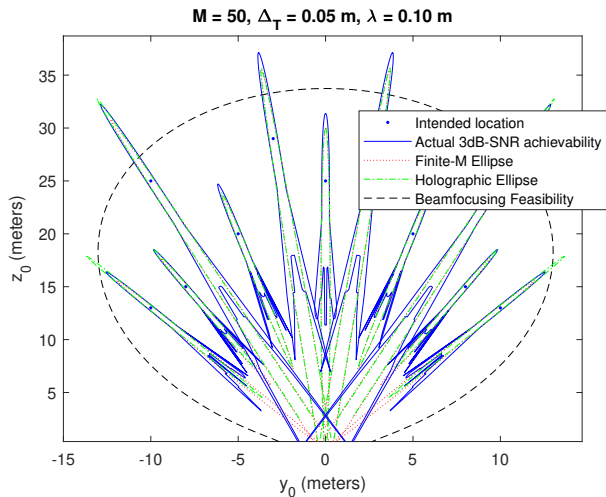


Fig. 7. Representation of the region that achieves an SNR at least 3dB below the optimum ($\kappa = 0.5$): true region (blue solid lines), finite- M second order approximation (red dotted lines) and holographic approximation (green dash-dotted lines) for different intended locations (markers).

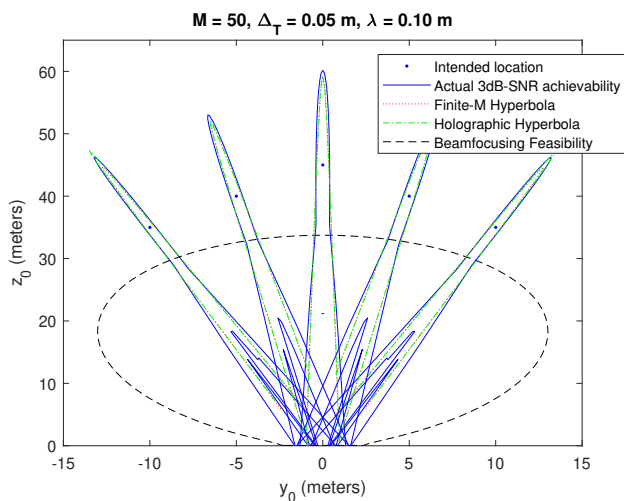


Fig. 8. Representation of the region that achieves an SNR at least 3dB below the optimum ($\kappa = 0.5$): true region (blue solid lines), finite- M second order approximation (red dotted lines) and holographic approximation (green dash-dotted lines) for different intended locations (markers).

quite accurate even for reasonably large values of the inter-element separation Δ_T .

Fig. 9 and Fig. 10 represent the actual achieved SNR when the transmitter is designed to guarantee a $\text{SNR}_0 = 10$ dB at a certain radial location for an elevation equal to $\theta = 0$ and $\theta = 30$ degrees respectively. The intended locations are represented by markers and the local quadratic approximations for fixed M and for the holographic regime are also shown in the same figure. Observe that the feasibility boundary can be used as the limit where beamfocusing can be safely used to multiplex signals in the radial domain. Beyond that point, the SNR loses its concavity and one cannot longer establish radial regions without mutual interference.

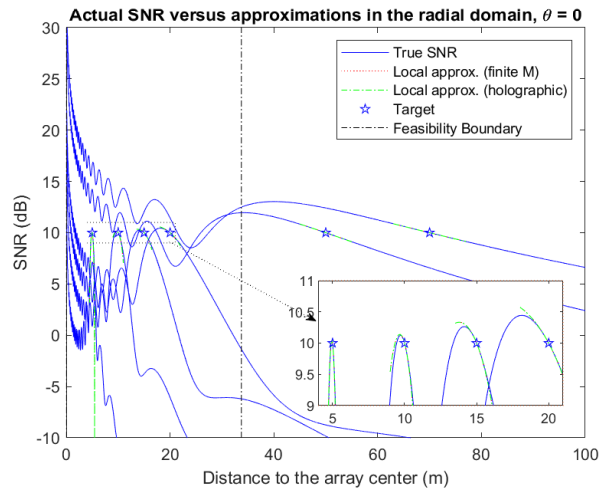


Fig. 9. Actual achieved SNR for different targeted spatial points (markers) assuming $\text{SNR}_0 = 10$ dB and a receiver located at $\theta = 0$ degrees. Local approximations are plotted in red dotted lines (finite M) and green dash-dotted lines (holographic).

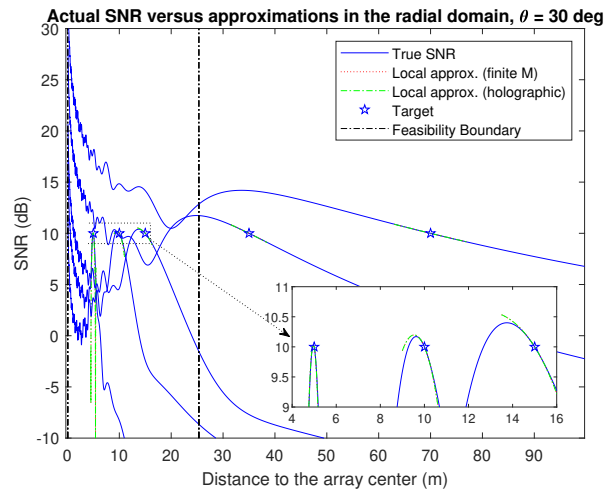


Fig. 10. Actual achieved SNR for different targeted spatial points (markers) assuming $\text{SNR}_0 = 10$ dB and a receiver located at $\theta = 30$ degrees. Local approximations are plotted in red dotted lines (finite M) and green dash-dotted lines (holographic).

V. CONCLUSIONS

The spatial region where beamfocusing is feasible by a ULA can be well characterized as the region where the SNR becomes locally concave. This means that the area close to the intended receiver that achieves a percentage of the maximum SNR can be asymptotically described as an ellipsoid. The holographic regime allows to characterize the beamfocusing feasibility region and provides some analytical insights into the shape and position of the coverage ellipsoids. According to the numerical analysis, the holographic description is quite accurate even in situations where the inter-element separation between consecutive elements of the ULA is moderately large. Furthermore, the asymptotic description is particularly useful in the region that is closer to the ULA, which corresponds to the area where beamfocusing is most effective.

APPENDIX A
PROOF OF PROPOSITION 1

We observe that we can express the complete 3×3 channel matrix associated to the m th transmit antenna as $\mathbf{H}_m(\mathbf{r}) = h_m(\mathbf{r})\mathbf{P}_m^\perp(\mathbf{r})$ where $h_m(\mathbf{r})$ is defined in (2). In this appendix, we will use the short hand notation $\mathbf{r}_m = \mathbf{r} - \mathbf{p}_m$, where we recall that \mathbf{r} is the position vector of the receiver and \mathbf{p}_m is the position vector of the m th antenna. Using these definitions, we can write $\mathbf{P}_m^\perp(\mathbf{r}) = \mathbf{I}_3 - \mathbf{r}_m\mathbf{r}_m^H/\|\mathbf{r}_m\|^2$.

A Taylor expansion of the i, j th entry of the channel matrix (denoted as $[\mathbf{H}_m(\mathbf{r})]_{i,j}$) can directly be expressed as

$$\begin{aligned} [\mathbf{H}_m(\mathbf{r})]_{i,j} &= [\mathbf{H}_m(\mathbf{r}_0)]_{i,j} + (\mathbf{r} - \mathbf{r}_0)^T \left[\frac{d[\mathbf{H}_m(\mathbf{r})]_{i,j}}{d\mathbf{r}} \right]_{\mathbf{r}=\mathbf{r}_0} \\ &+ \frac{1}{2} (\mathbf{r} - \mathbf{r}_0)^T \left[\frac{d^2[\mathbf{H}_m(\mathbf{r})]_{i,j}}{d\mathbf{r}d\mathbf{r}^T} \right]_{\mathbf{r}=\mathbf{r}_0} (\mathbf{r} - \mathbf{r}_0) + [\mathcal{R}_m(\bar{\mathbf{r}})]_{i,j} \end{aligned}$$

where $\mathcal{R}_m(\bar{\mathbf{r}}) = O(\|\mathbf{r} - \mathbf{r}_0\|^3)$ is the reminder matrix and $\bar{\mathbf{r}}$ is in the segment between \mathbf{r} and \mathbf{r}_0 . Let us write $\Delta_r = (\mathbf{r} - \mathbf{r}_0)$ and denote by $\mathcal{G}_m(\Delta_r)$ and $\mathcal{H}_m(\Delta_r)$ the 3×3 matrices defined as

$$\begin{aligned} [\mathcal{G}_m(\Delta_r)]_{i,j} &= (\mathbf{r} - \mathbf{r}_0)^T \left[\frac{d[\mathbf{H}_m(\mathbf{r})]_{i,j}}{d\mathbf{r}} \right]_{\mathbf{r}=\mathbf{r}_0} \\ [\mathcal{H}_m(\Delta_r)]_{i,j} &= \frac{1}{2} (\mathbf{r} - \mathbf{r}_0)^T \left[\frac{d^2[\mathbf{H}_m(\mathbf{r})]_{i,j}}{d\mathbf{r}d\mathbf{r}^T} \right]_{\mathbf{r}=\mathbf{r}_0} (\mathbf{r} - \mathbf{r}_0) \end{aligned}$$

so that we can write $\mathbf{H}_m(\mathbf{r}) = \mathbf{H}_m(\mathbf{r}_0) + \mathcal{G}_m(\Delta_r) + \mathcal{H}_m(\Delta_r) + \mathcal{R}_m(\bar{\mathbf{r}})$ and where $\mathcal{G}_m(\Delta_r) = O(\|\Delta_r\|)$ whereas $\mathcal{H}_m(\Delta_r) = O(\|\Delta_r\|^2)$ and $\mathcal{R}_m(\bar{\mathbf{r}}) = O(\|\Delta_r\|^3)$. In (6), we define $\mathcal{G}_{\text{pol}}(\Delta_r)$ and $\mathcal{H}_{\text{pol}}(\Delta_r)$ from $\mathcal{G}_m(\Delta_r)$ and $\mathcal{H}_m(\Delta_r)$ in the same way $\mathbf{H}_{\text{pol}}(\mathbf{r})$ is defined from $\mathbf{H}_m^{\text{pol}}(\mathbf{r})$, and $\mathcal{P}_{\text{pol}} = \mathcal{R}_{\text{pol}}/\|\Delta_r\|^3$ with \mathcal{R}_{pol} built up from the reminder matrices $\mathcal{R}_m(\bar{\mathbf{r}})$ in the same way. Next, we focus on the characterization of these three matrices, namely $\mathcal{G}_m(\Delta_r)$, $\mathcal{H}_m(\Delta_r)$ and $\mathcal{R}_m(\bar{\mathbf{r}})$. For the first two, we provide closed form analytical expressions. For the reminder, we simply reason how it can be uniformly bounded so that it is still of order $O(\|\Delta_r\|^3)$ in the holographic regime. The following lemma provides some useful identities that will be used throughout the derivations.

Lemma 1. *Let $h_m(\mathbf{r})$ be defined as in (2) and let $\mathbf{P}_m^\perp(\mathbf{r}) = \mathbf{I}_3 - \mathbf{P}_m(\mathbf{r})$, $\mathbf{P}_m(\mathbf{r}) = \mathbf{r}_m\mathbf{r}_m^H/\|\mathbf{r}_m\|^2$, where $\mathbf{r}_m = \mathbf{r} - \mathbf{p}_m$. With some abuse of notation, let r_k denote the k th component of \mathbf{r} and consider a 3-dimensional column vector \mathbf{a} with entries a_j . Then, we have*

$$\sum_k a_k \frac{\partial h_m(\mathbf{r})}{\partial r_k} = - \left(1 + j \frac{2\pi}{\lambda} \|\mathbf{r}_m\| \right) \frac{\mathbf{a}^T \mathbf{r}_m}{\|\mathbf{r}_m\|^2} h_m(\mathbf{r}) \quad (26)$$

$$\sum_k a_k \frac{\partial}{\partial r_k} \mathbf{P}_m^\perp(\mathbf{r}) = - \frac{\mathbf{r}_m \mathbf{a}^T}{\|\mathbf{r}_m\|^2} \mathbf{P}_m^\perp(\mathbf{r}) - \mathbf{P}_m^\perp(\mathbf{r}) \frac{\mathbf{a} \mathbf{r}_m^T}{\|\mathbf{r}_m\|^2} \quad (27)$$

$$\sum_k a_k \frac{\partial \|\mathbf{r}_m\|}{\partial r_k} = \frac{\mathbf{a}^T \mathbf{r}_m}{\|\mathbf{r}_m\|} \quad (28)$$

$$\sum_k a_k \frac{\partial}{\partial r_k} \frac{\mathbf{r}_m}{\|\mathbf{r}_m\|^2} = (\mathbf{I}_3 - 2\mathbf{P}_m(\mathbf{r})) \frac{\mathbf{a}}{\|\mathbf{r}_m\|^2}. \quad (29)$$

A. Computation of the gradient $\mathcal{G}_m(\Delta_r)$

Recall that $\mathbf{H}_m(\mathbf{r}) = h_m(\mathbf{r})\mathbf{P}_m^\perp(\mathbf{r})$. A direct application of (26)-(27) in Lemma 1 shows that, using the notation of the lemma,

$$\begin{aligned} \sum_k a_k \frac{\partial}{\partial r_k} \mathbf{H}_m(\mathbf{r}) &= - \left(1 + j \frac{2\pi}{\lambda} \|\mathbf{r}_m\| \right) \frac{\mathbf{a}^T \mathbf{r}_m}{\|\mathbf{r}_m\|^2} \mathbf{H}_m(\mathbf{r}) \\ &- \frac{\mathbf{r}_m \mathbf{a}^T}{\|\mathbf{r}_m\|^2} \mathbf{H}_m(\mathbf{r}) - \mathbf{H}_m(\mathbf{r}) \frac{\mathbf{a} \mathbf{r}_m^T}{\|\mathbf{r}_m\|^2}. \end{aligned} \quad (30)$$

The closed form expression of the gradient matrix $\mathcal{G}_m(\Delta_r)$ in (4) can be obtained by particularizing the above expression to $\mathbf{r} = \mathbf{r}_0$ and $\mathbf{a} = \Delta_r = \mathbf{r} - \mathbf{r}_0$, namely

$$\begin{aligned} \mathcal{G}_m(\Delta_r) &= - \left(1 + j \frac{2\pi}{\lambda} \|\mathbf{r}_{m,0}\| \right) \frac{\Delta_r^T \mathbf{r}_{m,0}}{\|\mathbf{r}_{m,0}\|^2} \mathbf{H}_m(\mathbf{r}_0) \\ &- \frac{\mathbf{r}_{m,0} \Delta_r^T}{\|\mathbf{r}_{m,0}\|^2} \mathbf{H}_m(\mathbf{r}_0) - \mathbf{H}_m(\mathbf{r}_0) \frac{\Delta_r \mathbf{r}_{m,0}^T}{\|\mathbf{r}_{m,0}\|^2} \end{aligned}$$

where now $\mathbf{r}_{m,0} = \mathbf{r}_0 - \mathbf{p}_m$.

B. Computation of the Hessian $\mathcal{H}_m(\Delta_r)$

Starting from the expression in (30) and using the identities in Lemma 1 we can directly obtain

$$\begin{aligned} \sum_{i,j} a_i b_j \frac{\partial^2 \mathbf{H}_m(\mathbf{r})}{\partial r_i \partial r_j} &= \frac{h_m(\mathbf{r})}{\|\mathbf{r}_m\|^2} \left[\Xi_1 + \left(1 + j \frac{2\pi}{\lambda} \|\mathbf{r}_m\| \right) \Xi_2 + \right. \\ &\left. + \left(1 + j \frac{2\pi}{\lambda} \|\mathbf{r}_m\| \right)^2 \Xi_3 \right] \quad (31) \end{aligned}$$

where the matrices Ξ_1 , Ξ_2 and Ξ_3 take the form

$$\begin{aligned} \Xi_1 &= -\mathbf{P}_m^\perp(\mathbf{r}) \left(\mathbf{b} \mathbf{a}^T + \mathbf{a} \mathbf{b}^T \right) \mathbf{P}_m^\perp(\mathbf{r}) \\ &+ \mathbf{P}_m(\mathbf{r}) \left(\mathbf{b} \mathbf{a}^T + \mathbf{a} \mathbf{b}^T \right) \mathbf{P}_m^\perp(\mathbf{r}) + \mathbf{P}_m^\perp(\mathbf{r}) \left(\mathbf{a} \mathbf{b}^T + \mathbf{b} \mathbf{a}^T \right) \mathbf{P}_m(\mathbf{r}) \\ &+ \left(\mathbf{b}^T \mathbf{P}_m(\mathbf{r}) \mathbf{a} \right) \mathbf{P}_m^\perp(\mathbf{r}) + 2 \left(\mathbf{a}^T \mathbf{P}_m^\perp(\mathbf{r}) \mathbf{b} \right) \mathbf{P}_m(\mathbf{r}) \\ \Xi_2 &= \mathbf{P}_m(\mathbf{r}) \left(\mathbf{a} \mathbf{b}^T + \mathbf{b} \mathbf{a}^T \right) \mathbf{P}_m^\perp(\mathbf{r}) + \mathbf{P}_m^\perp(\mathbf{r}) \left(\mathbf{b} \mathbf{a}^T + \mathbf{a} \mathbf{b}^T \right) \mathbf{P}_m(\mathbf{r}) \\ &- \mathbf{b}^T \mathbf{P}_m^\perp(\mathbf{r}) \mathbf{a} \mathbf{P}_m^\perp(\mathbf{r}) \\ \Xi_3 &= \mathbf{a}^T \mathbf{P}_m(\mathbf{r}) \mathbf{b} \mathbf{P}_m^\perp(\mathbf{r}). \end{aligned}$$

Hence, the expression for $\mathcal{H}_m(\Delta_r)$ can directly be obtained by particularizing the above expression to $\mathbf{r} = \mathbf{r}_0$ and $\mathbf{a} = \mathbf{b} = \Delta_r$, so that

$$\begin{aligned} \mathcal{H}_m(\Delta_r) &= \frac{h_m(\mathbf{r}_0)}{\|\mathbf{r}_{m,0}\|^2} \left[\Xi_{1,0} + \left(1 + j \frac{2\pi}{\lambda} \|\mathbf{r}_{m,0}\| \right) \Xi_{2,0} \right. \\ &\left. + \left(1 + j \frac{2\pi}{\lambda} \|\mathbf{r}_{m,0}\| \right)^2 \Xi_{3,0} \right] \end{aligned}$$

where we recall that $\mathbf{r}_{m,0} = \mathbf{r}_0 - \mathbf{p}_m$ and where the three matrices $\Xi_{1,0}$, $\Xi_{2,0}$, $\Xi_{3,0}$ take the form

$$\begin{aligned}\Xi_{1,0} &= -2\mathbf{P}_m^\perp(\mathbf{r}_0)\Delta_r\Delta_r^T\mathbf{P}_m^\perp(\mathbf{r}_0) \\ &\quad + 2\mathbf{P}_m(\mathbf{r}_0)\Delta_r\Delta_r^T\mathbf{P}_m^\perp(\mathbf{r}_0) + 2\mathbf{P}_m^\perp(\mathbf{r}_0)\Delta_r\Delta_r^T\mathbf{P}_m(\mathbf{r}_0) \\ &\quad + (\Delta_r^T\mathbf{P}_m(\mathbf{r}_0)\Delta_r)\mathbf{P}_m^\perp(\mathbf{r}_0) + 2(\Delta_r^T\mathbf{P}_m^\perp(\mathbf{r}_0)\Delta_r)\mathbf{P}_m(\mathbf{r}_0) \\ \Xi_{2,0} &= 2\mathbf{P}_m(\mathbf{r}_0)\Delta_r\Delta_r^T\mathbf{P}_m^\perp(\mathbf{r}_0) + 2\mathbf{P}_m^\perp(\mathbf{r}_0)\Delta_r\Delta_r^T\mathbf{P}_m(\mathbf{r}_0) \\ &\quad - (\Delta_r^T\mathbf{P}_m^\perp(\mathbf{r}_0)\Delta_r)\mathbf{P}_m^\perp(\mathbf{r}_0) \\ \Xi_{3,0} &= (\Delta_r^T\mathbf{P}_m(\mathbf{r}_0)\Delta_r)\mathbf{P}_m^\perp(\mathbf{r}_0).\end{aligned}$$

Once again, we can use the above expression to obtain a closed form analytical description of the product $\mathcal{H}_{\text{pol}}(\Delta_r)\mathbf{H}_{\text{pol}}^H(\mathbf{r}_0)$. Indeed, using again the polarization selection matrix \mathbf{E}_{pol} defined above, we can write

C. Analysis of the reminder $\mathcal{R}_m(\bar{\mathbf{r}})$

The objective of this section is to show that the spectral norm of the reminder term $\mathcal{R}_m(\bar{\mathbf{r}})$ can be bounded by a quantity of the type $P(\|\bar{\mathbf{r}} - \mathbf{p}_m\|^{-1})\|\Delta_r\|^3$, where $P(\cdot)$ is a polynomial with positive coefficients independent of the geometry of the problem (a nice polynomial, see Remark 1. In this appendix, the actual value of $P(\cdot)$ may vary from one line to the next. First of all, a direct application of (26)-(28) shows that

$$\sum c_k \frac{\partial}{\partial r_k} \frac{h_m(\mathbf{r})}{\|\mathbf{r}_m\|^2} = -\left(3 + \frac{2\pi j}{\lambda} \|\mathbf{r}_m\|\right) \frac{\mathbf{c}^T \mathbf{r}_m}{\|\mathbf{r}_m\|^4} h_m(\mathbf{r}).$$

Consequently, applying the chain rule for derivatives in (31) we find

$$\begin{aligned}&\sum_{i,j,k} a_i b_j c_k \frac{\partial^3 \mathbf{H}_m(\mathbf{r})}{\partial r_i \partial r_j \partial r_k} \\ &= -\left(3 + \frac{2\pi j}{\lambda} \|\mathbf{r}_m\|\right) \frac{\mathbf{c}^T \mathbf{r}_m}{\|\mathbf{r}_m\|^2} \sum_{i,j} a_i b_j \frac{\partial^2 \mathbf{H}_m(\mathbf{r})}{\partial r_i \partial r_j} \\ &\quad + \frac{h_m(\mathbf{r})}{\|\mathbf{r}_m\|^2} \left[\tilde{\Xi}_1 + \left(1 + \frac{2\pi j}{\lambda} \|\mathbf{r}_m\|\right) \tilde{\Xi}_2 + \left(1 + \frac{2\pi j}{\lambda} \|\mathbf{r}_m\|\right)^2 \tilde{\Xi}_3 \right] \\ &\quad + j \frac{2\pi}{\lambda} \frac{h_m(\mathbf{r}) \mathbf{c}^T \mathbf{r}_m}{\|\mathbf{r}_m\|^3} \left[\Xi_2 + 2 \left(1 + \frac{2\pi j}{\lambda} \|\mathbf{r}_m\|\right) \Xi_3 \right]\end{aligned}\quad (32)$$

where we have defined $\tilde{\Xi}_j = \sum c_k \partial \Xi_j / \partial r_k$. Now, from the expression of Ξ_1 , Ξ_2 , Ξ_3 we can easily reason that $\|\Xi_1\| \leq 9\|\mathbf{a}\|\|\mathbf{b}\|$, $\|\Xi_2\| \leq 5\|\mathbf{a}\|\|\mathbf{b}\|$ and $\|\Xi_3\| \leq \|\mathbf{a}\|\|\mathbf{b}\|$. On the other hand, we have $|h_m(\mathbf{r}_0)| = |\xi/\lambda| / \|\mathbf{r}_m\|$, which implies by the triangular inequality that

$$\begin{aligned}&\left\| \sum_{i,j} a_i b_j \frac{\partial^2 \mathbf{H}_m(\mathbf{r})}{\partial r_i \partial r_j} \right\| \leq \\ &\leq \frac{|\xi/\lambda|}{\|\mathbf{r}_m\|^3} \left[15 + \frac{14\pi}{\lambda} \|\mathbf{r}_m\| + \left(\frac{2\pi}{\lambda}\right)^2 \|\mathbf{r}_m\|^2 \right] \|\mathbf{a}\|\|\mathbf{b}\|\end{aligned}$$

whic can be expressed as $\|\mathbf{a}\|\|\mathbf{b}\|/\|\mathbf{r}_m\|P(\|\mathbf{r}_m\|^{-1})$. This shows that, since $\|\mathbf{c}^T \mathbf{r}_m\| \leq \|\mathbf{c}\|\|\mathbf{r}_m\|$ by Cauchy-Schwarz inequality, the modulus of the first term on the right hand side of (32) is upper bounded by $\|\mathbf{a}\|\|\mathbf{b}\|\|\mathbf{c}\|\|\mathbf{r}_m\|^{-1}P(\|\mathbf{r}_m\|^{-1})$.

A similar reasoning shows that the modulus of the third term on the right hand side of (32) is upper bounded by $\|\mathbf{a}\|\|\mathbf{b}\|\|\mathbf{c}\|$ times

$$\frac{2\pi}{\lambda} \frac{|\xi/\lambda|}{\|\mathbf{r}_m\|^3} \left(7 + \frac{4\pi}{\lambda} \|\mathbf{r}_m\|\right) = \frac{1}{\|\mathbf{r}_m\|^2} P(\|\mathbf{r}_m\|^{-1}).$$

It remains to bound the spectral norm of the matrices $\tilde{\Xi}_j$, $j = 1, 2, 3$. We have from (27) and the Cauchy-Schwarz inequality that $\|\sum c_k \partial \mathbf{P}_m(\mathbf{r}) / \partial r_k\| \leq 2\|\mathbf{c}\|\|\mathbf{r}_m\|^{-1}$. Therefore, by a direct application of the chain rule we find that $\|\tilde{\Xi}_j\| \leq k_j \|\mathbf{a}\|\|\mathbf{b}\|\|\mathbf{c}\| / \|\mathbf{r}_m\|$ where $k_1 = 24$, $k_2 = 12$ and $k_3 = 4$. This shows that the second term on the right hand side of (32) is upper bounded by $\|\mathbf{a}\|\|\mathbf{b}\|\|\mathbf{c}\|$ times

$$\frac{|\xi/\lambda|}{\|\mathbf{r}_m\|^4} \left[36 + \frac{28\pi}{\lambda} \|\mathbf{r}_m\| + \left(\frac{2\pi}{\lambda}\right)^2 \|\mathbf{r}_m\|^2 \right] = \frac{P(\|\mathbf{r}_m\|^{-1})}{\|\mathbf{r}_m\|^2}.$$

With all this, we can conclude that

$$\left\| \sum_{i,j,k} a_i b_j c_k \frac{\partial^3 \mathbf{H}_m(\mathbf{r})}{\partial r_i \partial r_j \partial r_k} \right\| \leq \|\mathbf{a}\|\|\mathbf{b}\|\|\mathbf{c}\| P\left(\frac{1}{\|\mathbf{r}_m\|}\right)$$

as we wanted to show.

APPENDIX B PROOF OF COROLLARY 1

We first observe that we can expand the product $\mathbf{H}_m(\mathbf{r})\mathbf{H}_m^H(\mathbf{r})$ as

$$\begin{aligned}\mathbf{H}_m(\mathbf{r})\mathbf{H}_m^H(\mathbf{r}) &= \mathbf{H}_m(\mathbf{r}_0)\mathbf{H}_m^H(\mathbf{r}_0) + \mathbf{H}_m(\mathbf{r}_0)\mathcal{G}_m^H(\Delta_r) \\ &\quad + \mathcal{G}_m(\Delta_r)\mathbf{H}_m^H(\mathbf{r}_0) + \mathcal{G}_m(\Delta_r)\mathcal{G}_m^H(\Delta_r) \\ &\quad + \mathcal{H}_m(\Delta_r)\mathbf{H}_m^H(\mathbf{r}_0) + \mathbf{H}_m(\mathbf{r}_0)\mathcal{H}_m^H(\Delta_r) + \Xi_m\end{aligned}$$

where we have introduced the error matrix

$$\begin{aligned}\Xi_m &= \mathcal{G}_m(\Delta_r)\mathcal{H}_m^H(\Delta_r) + \mathcal{H}_m(\Delta_r)\mathcal{G}_m^H(\Delta_r) \\ &\quad + \mathcal{R}_m(\bar{\mathbf{r}}, \Delta_r)(\mathbf{H}_m^H(\mathbf{r}_0) + \mathcal{G}_m^H(\Delta_r) + \mathcal{H}_m^H(\Delta_r)) \\ &\quad + (\mathbf{H}_m(\mathbf{r}_0) + \mathcal{G}_m(\Delta_r) + \mathcal{H}_m(\Delta_r))\mathcal{R}_m^H(\bar{\mathbf{r}}, \Delta_r) \\ &\quad + \mathcal{H}_m(\Delta_r)\mathcal{H}_m^H(\Delta_r) + \mathcal{R}_m(\bar{\mathbf{r}}, \Delta_r)\mathcal{R}_m^H(\bar{\mathbf{r}}, \Delta_r).\end{aligned}$$

We only need to show that $\|\Xi_m\| < K\|\Delta_r\|^3$ where K is a nice constant. We recall here that we can write $\|\mathbf{H}_m(\mathbf{r}_0)\| \leq P(\|\mathbf{r}_{m,0}\|^{-1})$, $\|\mathcal{G}_m(\Delta_r)\| \leq P(\|\mathbf{r}_{m,0}\|^{-1})\|\Delta_r\|$, $\|\mathcal{H}_m(\Delta_r)\| \leq P(\|\mathbf{r}_{m,0}\|^{-1})\|\Delta_r\|^2$ and $\mathcal{R}_m(\bar{\mathbf{r}}, \Delta_r) \leq P(\|\bar{\mathbf{r}}_{m,0}\|^{-1})\|\Delta_r\|^2$. Hence, using the fact that $\|\mathbf{A} + \mathbf{B}\| \leq \|\mathbf{A}\| + \|\mathbf{B}\|$ and $\|\mathbf{AB}\| \leq \|\mathbf{A}\|\|\mathbf{B}\|$ we can readily see that $\|\Xi_m\| / \|\Delta_r\|^3$ is upper bounded by a term of the form

$$P(\|\mathbf{r}_{m,0}\|^{-1}) + P(\|\mathbf{r}_{m,0}\|^{-1})P(\|\bar{\mathbf{r}}_{m,0}\|^{-1}) + P(\|\bar{\mathbf{r}}_{m,0}\|^{-1})$$

where we recall that the nice polynomials $P(\cdot)$ may take on a different value at each appearance. Now observe that $\|\mathbf{r}_{m,0}\| > z_0$, $\|\bar{\mathbf{r}}_{m,0}\| > \min\{z, z_0\}$ and so that $\|\Xi_m\| \leq K\|\Delta_r\|^3$ where K is a nice constant.

APPENDIX C
PROOF OF PROPOSITION 2

It is well known that when $x_0 = 0$ the eigenvector associated to the maximum eigenvalue of the matrix

$$\frac{1}{2M+1} \mathbf{H}_{\text{pol}}(\mathbf{r}_0) \mathbf{H}_{\text{pol}}^H(\mathbf{r}_0)$$

is equal to the first column of a 3×3 identity matrix, denoted by $\mathbf{u} = \mathbf{e}_1$. This was proven in [34] for $t_{\text{pol}} = 3$ and $t_{\text{pol}} = 2$ (the result for $t_{\text{pol}} = 1$ is trivial since the above matrix has zeros everywhere except for the (1,1)th entry). Using the fact that $\mathbf{u} = \mathbf{e}_1$ we see that only the first column of the two error matrices $\mathcal{G}_{\text{pol}}(\Delta_r) \mathbf{H}_{\text{pol}}^H(\mathbf{r}_0) / (2M+1)$ and $\mathcal{H}_{\text{pol}}(\Delta_r) \mathbf{H}_{\text{pol}}^H(\mathbf{r}_0) / (2M+1)$ come into play, which leads to a considerable simplification of the above expression. To provide a closed form expression for the matrix $\mathcal{G}_{\text{pol}}(\Delta_r) \mathbf{H}_{\text{pol}}^H(\mathbf{r}_0)$, let \mathbf{E}_{pol} denote a 3×3 diagonal selection matrix that contains ones at the t_{pol} first diagonal entries and zeros elsewhere. Using the expression of $\mathcal{G}_m(\Delta_r)$ in (4) we can express

$$\begin{aligned} \mathcal{G}_{\text{pol}}(\Delta_r) \mathbf{H}_{\text{pol}}^H(\mathbf{r}_0) &= \sum_{m=-M}^M \mathcal{G}_m(\Delta_r) \mathbf{E}_{\text{pol}} \mathbf{H}_m^H(\mathbf{r}_0) \\ &= - \left| \frac{\xi}{\lambda} \right|^2 \sum_{m=-M}^M \left[\frac{\mathbf{r}_{m,0} \Delta_r^T \mathbf{P}_m^\perp(\mathbf{r}_0) + \mathbf{P}_m^\perp(\mathbf{r}_0) \Delta_r \mathbf{r}_{m,0}^T}{\|\mathbf{r}_{m,0}\|^4} \times \right. \\ &\quad \left. \times \mathbf{E}_{\text{pol}} \mathbf{P}_m^\perp(\mathbf{r}_0) \right. \\ &\quad \left. + \frac{\Delta_r^T \mathbf{r}_{m,0}}{\|\mathbf{r}_{m,0}\|^4} \left(1 + j \frac{2\pi}{\lambda} \|\mathbf{r}_{m,0}\| \right) \mathbf{P}_m^\perp(\mathbf{r}_0) \mathbf{E}_{\text{pol}} \mathbf{P}_m^\perp(\mathbf{r}_0) \right] \end{aligned} \quad (33)$$

where we have used the fact that $|h_m(\mathbf{r}_0)|^2 = |\xi/\lambda|^2 / \|\mathbf{r}_{m,0}\|^2$ and we recall that $\mathbf{r}_{m,0} = \mathbf{r}_0 - \mathbf{p}_m$. Regarding the expression for $\mathcal{H}_{\text{pol}}(\Delta_r) \mathbf{H}_{\text{pol}}^H(\mathbf{r}_0)$, we can similarly use the expression of $\mathcal{H}_m(\Delta_r)$ in (5) to see that

$$\begin{aligned} \mathcal{H}_{\text{pol}}(\Delta_r) \mathbf{H}_{\text{pol}}^H(\mathbf{r}_0) &= \sum_{m=-M}^M \mathcal{H}_m(\Delta_r) \mathbf{E}_{\text{pol}} \mathbf{H}_m^H(\mathbf{r}_0) \\ &= \sum_{m=-M}^M \frac{|\xi/\lambda|^2}{\|\mathbf{r}_{m,0}\|^4} \left[\mathbf{\Xi}_{1,0} + \left(1 + j \frac{2\pi}{\lambda} \|\mathbf{r}_{m,0}\| \right) \mathbf{\Xi}_{2,0} \right. \\ &\quad \left. + \left(1 + j \frac{2\pi}{\lambda} \|\mathbf{r}_{m,0}\| \right)^2 \mathbf{\Xi}_{3,0} \right] \mathbf{E}_{\text{pol}} \mathbf{P}_m^\perp(\mathbf{r}_0). \end{aligned} \quad (34)$$

where the matrices $\mathbf{\Xi}_{j,0}$ are defined in the statement of Proposition 1. To further simplify these expressions, we use the fact that $\mathbf{P}_m^\perp(\mathbf{r}_0) \mathbf{e}_1 = \mathbf{e}_1$ and $\mathbf{P}_m(\mathbf{r}_0) \mathbf{e}_1 = 0$. Furthermore, $\mathbf{E}_{\text{pol}} \mathbf{e}_1 = \mathbf{e}_1$ because the polarization along the x -axis is assumed to be always employed. These properties allow to simplify the expression in (33) into

$$\frac{1}{2M+1} \mathcal{G}_{\text{pol}}(\Delta_r) \mathbf{H}_{\text{pol}}^H(\mathbf{r}_0) \mathbf{u} = |\xi/\lambda|^2 \mathbb{G} \Delta_r \quad (35)$$

where

$$\mathbb{G} = \begin{bmatrix} 0 & \bar{s}_M^{(3)} + j \frac{2\pi}{\lambda} \bar{s}_M^{(2)} & -s_M^{(4)} z_0 - j \frac{2\pi}{\lambda} s_M^{(3)} z_0 \\ \bar{s}_M^{(3)} & 0 & 0 \\ -z_0 s_M^{(4)} & 0 & 0 \end{bmatrix}$$

Likewise, using the expression in (34) we immediately obtain

$$\begin{aligned} &\mathcal{H}_{\text{pol}}(\Delta_r) \mathbf{H}_{\text{pol}}^H(\mathbf{r}_0) \mathbf{u} \\ &= -\Delta_x \left| \frac{\xi}{\lambda} \right|^2 \sum_{m=-M}^M \frac{1}{\|\mathbf{r}_0 - \mathbf{p}_m\|^4} \mathbf{P}_m^\perp \Delta_r \\ &\quad + \Delta_x \left| \frac{\xi}{\lambda} \right|^2 \sum_{m=-M}^M \frac{1}{\|\mathbf{r}_0 - \mathbf{p}_m\|^4} \left(2 + j \frac{2\pi}{\lambda} \|\mathbf{r}_0 - \mathbf{p}_m\| \right) \mathbf{P}_m(\mathbf{r}_0) \Delta_r \\ &\quad + \frac{|\xi/\lambda|^2}{2} \sum_{m=-M}^M \left[1 + \left(1 + j \frac{2\pi}{\lambda} \|\mathbf{r}_0 - \mathbf{p}_m\| \right)^2 \right] \times \\ &\quad \times \frac{\Delta_r^T \mathbf{P}_m(\mathbf{r}_0) \Delta_r}{\|\mathbf{r}_0 - \mathbf{p}_m\|^4} \mathbf{u} \\ &\quad - \frac{|\xi/\lambda|^2}{2} \sum_{m=-M}^M \left(1 + j \frac{2\pi}{\lambda} \|\mathbf{r}_0 - \mathbf{p}_m\| \right) \frac{\Delta_r^T \mathbf{P}_m^\perp(\mathbf{r}_0) \Delta_r}{\|\mathbf{r}_0 - \mathbf{p}_m\|^4} \mathbf{u}. \end{aligned}$$

At this point, we can use the expression of $\mathbf{P}_m^\perp(\mathbf{r}_0)$ so that

$$\begin{aligned} &\frac{1}{2M+1} \mathcal{H}_{\text{pol}}(\Delta_r) \mathbf{H}_{\text{pol}}^H(\mathbf{r}_0) \mathbf{u} = \\ &= \Delta_x |\xi/\lambda|^2 \mathbb{H}_1 \Delta_r + \frac{|\xi/\lambda|^2}{2} \Delta_r^T \mathbb{H}_2 \Delta_r \mathbf{u} \end{aligned} \quad (36)$$

where we have introduced the two matrices

$$\begin{aligned} \mathbb{H}_1 &= \begin{bmatrix} -s_M^{(4)} & 0 & 0 \\ 0 & 2s_M^{(4)} - 3z_0^2 s_M^{(6)} & -3\bar{s}_M^{(5)} z_0 \\ 0 & -3\bar{s}_M^{(5)} z_0 & -s_M^{(4)} + 3z_0^2 s_M^{(6)} \end{bmatrix} \\ &\quad + \frac{2\pi j}{\lambda} \begin{bmatrix} 0 & 0 & 0 \\ 0 & s_M^{(3)} - z_0^2 s_M^{(5)} & -\bar{s}_M^{(4)} z_0 \\ 0 & -\bar{s}_M^{(4)} z_0 & z_0^2 s_M^{(5)} \end{bmatrix} \\ \mathbb{H}_2 &= \begin{bmatrix} -s_M^{(4)} & 0 & 0 \\ 0 & 2s_M^{(4)} - 3z_0^2 s_M^{(6)} & -3\bar{s}_M^{(5)} z_0 \\ 0 & -3z_0 \bar{s}_M^{(5)} & 3s_M^{(6)} z_0^2 - s_M^{(4)} \end{bmatrix} \\ &\quad + \left(\frac{2\pi}{\lambda} \right)^2 \begin{bmatrix} 0 & 0 & 0 \\ 0 & z_0^2 s_M^{(4)} - s_M^{(2)} & \bar{s}_M^{(3)} z_0 \\ 0 & \bar{s}_M^{(3)} z_0 & -z_0^2 s_M^{(4)} \end{bmatrix} \\ &\quad + \frac{2\pi j}{\lambda} \begin{bmatrix} -s_M^{(3)} & 0 & 0 \\ 0 & 2s_M^{(3)} - 3z_0^2 s_M^{(5)} & -3\bar{s}_M^{(4)} z_0 \\ 0 & -3\bar{s}_M^{(4)} z_0 & 3z_0^2 s_M^{(5)} - s_M^{(3)} \end{bmatrix}. \end{aligned}$$

Now, using (35) and (36) into (12), we can conclude that

$$\begin{aligned} \text{SNR}(\mathbf{r}) &= \text{SNR}(\mathbf{r}_0) + \text{SNR}(\mathbf{r}_0) \frac{1}{s_M^{(2)}} (\Delta_r^T \mathbb{G}^H \mathbf{u} + \mathbf{u}^H \mathbb{G} \Delta_r) \\ &\quad + \text{SNR}(\mathbf{r}_0) \frac{1}{s_M^{(2)}} \Delta_x (\Delta_r^T \mathbb{H}_1^H \mathbf{u} + \mathbf{u}^H \mathbb{H}_1 \Delta_r) \\ &\quad + \text{SNR}(\mathbf{r}_0) \Delta_r^T \left[\frac{\mathbb{G}^H \mathbb{G}}{(s_M^{(2)})^2} + \frac{\mathbb{H}_2 + \mathbb{H}_2^H}{2s_M^{(2)}} \right] \Delta_r + \epsilon_M \end{aligned}$$

where we have used the fact that $\lambda_{\text{max}} = |\xi/\lambda|^2 s_M^{(2)}$ and $\text{SNR}(\mathbf{r}_0) = P \lambda_{\text{max}} / \sigma^2$. Using the expression of \mathbb{G} , \mathbb{H}_1 and

\mathbb{H}_2 we can compactly express the above expression as in (13) where

$$\begin{aligned} \mathbf{m}_M &= -\frac{1}{s_M^{(2)}} \text{Re}[\mathbf{G}] \mathbf{u} \\ \mathcal{M}_M &= -\frac{1}{\left(s_M^{(2)}\right)^2} \text{Re}[\mathbf{G}^H \mathbf{G}] - \frac{1}{2s_M^{(2)}} (\mathbb{H}_2 + \mathbb{H}_2^H) \\ &\quad - \frac{1}{s_M^{(2)}} (\mathbb{H}_1^H \mathbf{u} \mathbf{u}^H + \mathbf{u} \mathbf{u}^H \mathbb{H}_1) \end{aligned}$$

which correspond to the expressions given in the statement of the proposition. The only remaining point is to prove that $\gamma_M^{(1)} \geq 0$. To see this, we can use the Cauchy-Schwarz inequality to show that

$$s_M^{(2k)} s_M^{(2l)} \geq \left(s_M^{(k+l)}\right)^2 \quad (37)$$

$$s_M^{2k} \left(s_M^{2(l-1)} - z_0^2 s_M^{(2l)}\right) \geq \left(\bar{s}_M^{k+l-1}\right)^2 \quad (38)$$

for any $k, l \in \mathbb{N}$. To see that $\gamma_M^{(1)} > 0$, use (37)-(38) with $k = 1, l = 3$ so that $s_M^{(2)} s_M^{(6)} \geq \left(s_M^{(4)}\right)^2$ and $s_M^{(2)} \left(s_M^{(4)} - z_0^2 s_M^{(6)}\right) \geq \left(\bar{s}_M^{(3)}\right)^2$. Applying these two inequalities consecutively, we find $\gamma_M^{(1)} = \left(3s_M^{(2)} s_M^{(4)} - \left(\bar{s}_M^{(3)}\right)^2 - z_0^2 \left(s_M^{(4)}\right)^2\right) / \left(s_M^{(2)}\right)^2 \geq \left(3s_M^{(2)} s_M^{(4)} - \left(\bar{s}_M^{(3)}\right)^2 - z_0^2 s_M^{(2)} s_M^{(6)}\right) / \left(s_M^{(2)}\right)^2 \geq 2\left(s_M^{(2)} s_M^{(4)}\right) / \left(s_M^{(2)}\right)^2 > 0$.

REFERENCES

- [1] S. Priebe and T. Kurner, "Stochastic modeling of THz indoor radio channels," *IEEE Transactions on Wireless Communications*, vol. 12, no. 9, pp. 4445–4455, 2013.
- [2] M. Shafi, J. Zhang, H. Tataria, A. F. Molisch, S. Sun, T. S. Rappaport, F. Tufvesson, S. Wu, and K. Kitao, "Microwave vs. millimeter-wave propagation channels: Key differences and impact on 5G cellular systems," *IEEE Communications Magazine*, vol. 56, no. 12, pp. 14–20, 2018.
- [3] P. Driessen and G. Foschini, "On the capacity formula for multiple input-multiple output wireless channels: a geometric interpretation," *IEEE Transactions on Communications*, vol. 47, no. 2, pp. 173–176, 1999.
- [4] J.-S. Jiang and M. Ingram, "Spherical-wave model for short-range MIMO," *IEEE Transactions on Communications*, vol. 53, no. 9, pp. 1534–1541, 2005.
- [5] F. Bohagen, P. Orten, and G. E. Oien, "On spherical vs. plane wave modeling of line-of-sight MIMO channels," *IEEE Transactions on Communications*, vol. 57, no. 3, pp. 841–849, 2009.
- [6] L. Sanguinetti, A. A. D'Amico, and M. Debbah, "Wavenumber-division multiplexing in line-of-sight holographic MIMO communications," *IEEE Transactions on Wireless Communications*, vol. 22, no. 4, pp. 2186–2201, 2023.
- [7] H. Zhang, N. Shlezinger, F. Guidi, D. Dardari, and Y. C. Eldar, "6g wireless communications: From far-field beam steering to near-field beam focusing," *IEEE Communications Magazine*, vol. 61, no. 4, pp. 72–77, 2023.
- [8] E. Björnson, C.-B. Chae, R. W. Heath Jr, T. L. Marzetta, A. Mezghani, L. Sanguinetti, F. Rusek, M. R. Castellanos, D. Jun, and Ö. T. Demir, "Towards 6G MIMO: Massive spatial multiplexing, dense arrays, and interplay between electromagnetics and processing," *arXiv preprint arXiv:2401.02844*, 2024.
- [9] Y. Liu, Z. Wang, J. Xu, C. Ouyang, X. Mu, and R. Schober, "Near-field communications: A tutorial review," *IEEE Open Journal of the Communications Society*, vol. 4, pp. 1999–2049, 2023.
- [10] P. Ramezani and E. Björnson, *Near-Field Beamforming and Multiplexing Using Extremely Large Aperture Arrays*. Cham: Springer International Publishing, 2024, pp. 317–349.
- [11] N. J. Myers and R. W. Heath, "Infocus: A spatial coding technique to mitigate misfocus in near-field los beamforming," *IEEE Transactions on Wireless Communications*, vol. 21, no. 4, pp. 2193–2209, 2022.
- [12] Z. Wu and L. Dai, "Multiple access for near-field communications: Sdma or Idma?" *IEEE Journal on Selected Areas in Communications*, vol. 41, no. 6, pp. 1918–1935, 2023.
- [13] A. Kosasih and E. Björnson, "Finite beam depth analysis for large arrays," *IEEE Transactions on Wireless Communications*, vol. 23, no. 8, pp. 10 015–10 029, 2024.
- [14] E. Björnson, O. T. Demir, and L. Sanguinetti, "A primer on near-field beamforming for arrays and reconfigurable intelligent surfaces," in *2021 55th Asilomar Conference on Signals, Systems, and Computers*, 2021, pp. 105–112.
- [15] L. Wei, C. Huang, G. C. Alexandropoulos, Z. Yang, J. Yang, W. E. I. Sha, Z. Zhang, M. Debbah, and C. Yuen, "Tri-polarized holographic MIMO surfaces for near-field communications: Channel modeling and precoding design," *IEEE Trans. on Wireless Comms.*, pp. 1–1, 2023.
- [16] T. Gong, L. Wei, C. Huang, G. C. Alexandropoulos, M. Debbah, and C. Yuen, "Near-field channel modeling for holographic MIMO communications," *IEEE Wireless Communications*, vol. 31, no. 3, pp. 108–116, 2024.
- [17] A. Agustin and X. Mestre, "Near-field beamfocusing with polarized antennas," in *2024 IEEE Wireless Communications and Networking Conference (WCNC)*, 2024, pp. 01–06.
- [18] A. Poon, R. Brodersen, and D. Tse, "Degrees of freedom in multiple-antenna channels: a signal space approach," *IEEE Transactions on Information Theory*, vol. 51, no. 2, pp. 523–536, 2005.
- [19] M. F. Imani, J. N. Gollub, O. Yurduseven, A. V. Diebold, M. Boyarsky, T. Fromenteze, L. Pulido-Mancera, T. Sleasman, and D. R. Smith, "Review of metasurface antennas for computational microwave imaging," *IEEE Transactions on Antennas and Propagation*, vol. 68, no. 3, pp. 1860–1875, 2020.
- [20] G. Lipworth, A. Mrozack, J. Hunt, D. L. Marks, T. Driscoll, D. Brady, and D. R. Smith, "Metamaterial apertures for coherent computational imaging on the physical layer," *J. Opt. Soc. Am. A*, vol. 30, no. 8, pp. 1603–1612, Aug 2013.
- [21] G. Lipworth, A. Rose, O. Yurduseven, V. R. Gowda, M. F. Imani, H. Odabasi, P. Trofater, J. Gollub, and D. R. Smith, "Comprehensive simulation platform for a metamaterial imaging system," *Appl. Opt.*, vol. 54, no. 31, pp. 9343–9353, Nov 2015.
- [22] D. R. Smith, O. Yurduseven, L. P. Mancera, P. Bowen, and N. B. Kundtz, "Analysis of a waveguide-fed metasurface antenna," *Phys. Rev. Appl.*, vol. 8, p. 054048, Nov 2017.
- [23] M. F. Imani, T. Sleasman, and D. R. Smith, "Two-dimensional dynamic metasurface apertures for computational microwave imaging," *IEEE Antennas and Wireless Propagation Letters*, vol. 17, no. 12, pp. 2299–2303, 2018.
- [24] D. Dardari and N. Decarli, "Holographic communication using intelligent surfaces," *IEEE Communications Magazine*, vol. 59, no. 6, pp. 35–41, 2021.
- [25] C. Huang, S. Hu, G. C. Alexandropoulos, A. Zappone, C. Yuen, R. Zhang, M. D. Renzo, and M. Debbah, "Holographic MIMO surfaces for 6g wireless networks: Opportunities, challenges, and trends," *IEEE Wireless Communications*, vol. 27, no. 5, pp. 118–125, 2020.
- [26] T. Gong, P. Gavrilidis, R. Ji, C. Huang, G. C. Alexandropoulos, L. Wei, Z. Zhang, M. Debbah, H. V. Poor, and C. Yuen, "Holographic MIMO communications: Theoretical foundations, enabling technologies, and future directions," *IEEE Communications Surveys & Tutorials*, vol. 26, no. 1, pp. 196–257, 2024.
- [27] A. Pizzo, L. Sanguinetti, and T. L. Marzetta, "Fourier plane-wave series expansion for holographic MIMO communications," *IEEE Transactions on Wireless Communications*, vol. 21, no. 9, pp. 6890–6905, 2022.
- [28] A. Sayeed and N. Behdad, "Continuous aperture phased MIMO: Basic theory and applications," in *2010 48th Annual Allerton Conference on Communication, Control, and Computing*, 2010, pp. 1196–1203.
- [29] A. M. Sayeed and N. Behdad, "Continuous aperture phased MIMO: A new architecture for optimum line-of-sight links," in *2011 IEEE International Symposium on Antennas and Propagation (APSURSI)*, 2011, pp. 293–296.
- [30] S. Hu, F. Rusek, and O. Edfors, "Beyond massive MIMO: The potential of data transmission with large intelligent surfaces," *IEEE Transactions on Signal Processing*, vol. 66, no. 10, pp. 2746–2758, 2018.
- [31] A. Agustin and X. Mestre, "Exploiting multiple polarizations in extra large holographic mimo," *Submitted to IEEE Transactions on Wireless Communications*, 2024. [Online]. Available: <https://arxiv.org/abs/2410.08839>
- [32] J. L. Coolidge, *A history of the Conic Sections and Quadric Surfaces*. New York: Dover Publications, 1968.
- [33] E. Björnson, O. T. Demir, and L. Sanguinetti, "A primer on near-field beamforming for arrays and reconfigurable intelligent surfaces," 2021.
- [34] X. Mestre and A. Agustin, "Available degrees of spatial multiplexing of a uniform linear array with multiple polarizations: A holographic perspective," *IEEE Open Journal on Signal Processing*, 2025.